

Certified Gradient-Based Contact-Rich Manipulation via Smoothing-Error Reachable Tubes

Wei-Chen Li and Glen Chou

Georgia Institute of Technology, Atlanta, Georgia 30308

Email: {wli777, chou}@gatech.edu

Abstract—Gradient-based methods can efficiently optimize controllers using physical priors and differentiable simulators, but contact-rich manipulation remains challenging due to discontinuous or vanishing gradients from hybrid contact dynamics. Smoothing the dynamics yields continuous gradients, but the resulting model mismatch can cause controller failures when executed on real systems. We address this trade-off by planning with smoothed dynamics while explicitly quantifying and compensating for the induced errors, providing formal guarantees of constraint satisfaction and goal reachability on the true hybrid dynamics. Our method smooths both contact dynamics and geometry via a novel differentiable simulator based on convex optimization, which enables us to characterize the discrepancy from the true dynamics as a set-valued deviation. This deviation constrains the optimization of time-varying affine feedback policies through analytical bounds on the system’s reachable set, enabling robust constraint satisfaction guarantees for the true closed-loop hybrid dynamics, while relying solely on informative gradients from the smoothed dynamics. We evaluate our method on several contact-rich tasks, including planar pushing, object rotation, and in-hand dexterous manipulation, achieving guaranteed constraint satisfaction with lower safety violation and goal error than baselines. By bridging differentiable physics with set-valued robust control, our method is the first certifiable gradient-based policy synthesis method for contact-rich manipulation.

I. INTRODUCTION

Contact-rich manipulation involves controlling unactuated objects to reach a desired configuration, which requires making discrete decisions about when and how to make or break contact. Among current approaches, reinforcement learning (RL) [48] and zero-order planning methods such as cross-entropy method (CEM) [18, 30], covariance matrix adaptation evolution strategy (CMA-ES) [16, 21], and model predictive path integral (MPPI) control [44] have achieved notable success. However, these methods are fundamentally sampling-based and effectively require rediscovering the underlying physics through trial-and-error, resulting in low sample efficiency.

In contrast, gradient-based trajectory optimization [8, 47, 32] can exploit the problem’s physical structure via differentiable simulation [40, 39]. However, hybrid dynamics in contact-rich manipulation violate key assumptions of these methods. In particular, nonsmooth contact dynamics create fundamental challenges: gradients are often discontinuous across contact modes and frequently zero. For example, before the robot contacts the object, its actions do not affect the object or reward. Since the contact manifold occupies a zero-measure subset of the configuration space, standard gradients provide little guidance for improving actions. As such, while

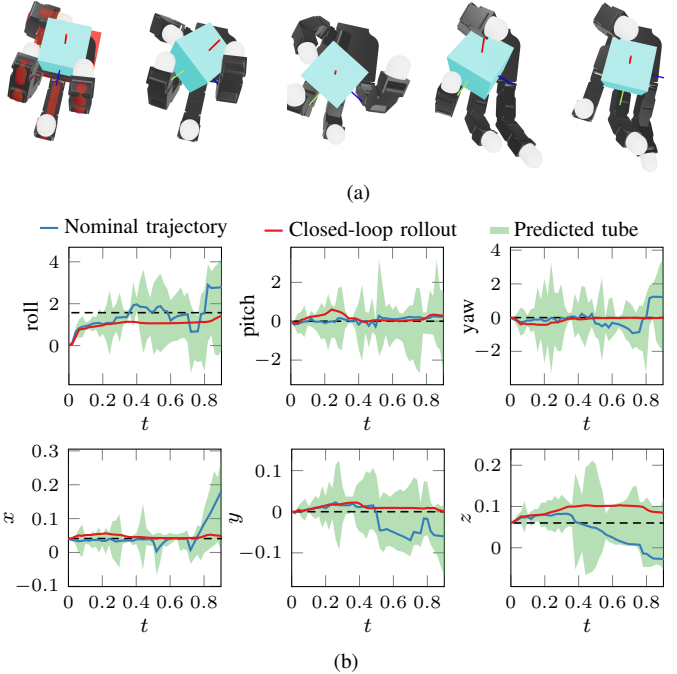


Figure 1. We evaluate on a in-hand cube reorientation task. (a) Keyframes from the executed rollout. (b) The closed-loop trajectory stays within the reachable tube for all object DoF, validating the constraint satisfaction guarantees. Guiding planning with these tubes allows the smoothed dynamics to strategically overshoot the target to compensate for model mismatch, ensuring low goal error on the true hybrid dynamics.

differentiable simulators exist [12], the practical utility of the gradients they provide remains limited [53] for manipulation.

From the RL policy gradient formula [54] with policy π_θ ,

$$\nabla_\theta J(\theta) := \mathbb{E}_{\tau \sim \pi_\theta} [\nabla_\theta \log p_\theta(\tau) R(\tau)],$$

it might appear that the policy gradient $\nabla_\theta J(\theta)$ would also vanish, as most actions do not affect the manipulated object and yield zero episodic reward $R(\tau)$ for a sampled trajectory τ . RL addresses this through stochasticity in the policy and environment, often via domain randomization [43, 46], so that some rollouts accidentally induce contact, producing nonzero rewards and gradients. Domain randomization can be seen as randomized smoothing, where the dynamics are convolved with a probabilistic kernel to improve the optimization landscape [52]. Later work showed that this is equivalent to analytical smoothing [42, 58], where the environment is deterministic but contact dynamics are smoothed explicitly.

Despite the connection between RL and analytically-smoothed contact dynamics, naively planning with smoothed

dynamics often fails due to premature contact loss [49] arising from the unilateral nature of contact, i.e., contact can only apply normal forces in one direction. Later work mitigates this issue by creating a local contact trust region (CTR) [51], replacing conventional elliptical trust regions [50] to keep smoothed dynamics close to the true hybrid system. However, contact loss can still occur, and the CTR is heuristic, as the allowable deviation that ensures a sufficiently accurate model for planning is not formally characterized. Quantifying and propagating smoothing error through the true hybrid dynamics produces reachable sets that can constrain controllers to ensure goal reachability and constraint satisfaction, which is critical for high-precision manipulation. However, no methods can 1) quantify smoothing error, 2) perform reachability analysis for high-dimensional hybrid contact dynamics, and 3) perform efficient gradient-based policy optimization using these bounds.

To close these gaps, we propose a scalable *robust manipulation planner* that tightly bounds smoothing error, propagates it through the true hybrid dynamics, and leverages the resulting reachable tubes to guarantee task constraint satisfaction and goal reaching. A key ingredient enabling scalability is a novel, principled *differentiable simulator* that smooths contact and geometry in a modular manner via convex optimization. This simulator provides informative gradients for planning, as well as gradients with respect to the smoothing parameter κ , which are required to compute smoothing-error bounds. *Our key insight is that the deviation between the smoothed dynamics and the true hybrid dynamics can be treated as a structured model mismatch, which we show can be tightly bounded by a set-valued, state-control-dependent function.* Building on recent advances in set-valued robust control [29], we jointly optimize a nominal trajectory and an affine feedback policy that yield analytical bounds of the true hybrid system behavior under feedback control. We compare with CTR in Section V-C, obtaining similar solve times while reducing constraint violations and certifying constraint satisfaction on the *true system* via reachability analysis. Our contributions are:

- 1) We present a differentiable simulator with built-in contact and geometry smoothing which is built from modular differentiable convex programs, providing accurate gradients for planning and smoothing error bounding, without differentiating through the entire computation graph.
- 2) We derive tight analytical bounds on the deviation between smoothed dynamics and true hybrid dynamics, which depend on gradients provided by our differentiable simulator.
- 3) We propose a robust policy synthesis method that uses gradients from the smoothed dynamics for efficient optimization while using tube-valued predictions of the true hybrid dynamics under feedback control to ensure robust constraint satisfaction. Through this process, we characterize what constitutes informative gradients for action refinement in contact-rich manipulation.
- 4) We show the efficacy of our method on contact-rich manipulation problems both in simulation and on hardware, including planar pushing (2DOF), bimanual

non-prehensile manipulation (9DOF), and dexterous in-hand reorientation (22DOF), reducing constraint violation rate relative to baselines.

II. RELATED WORK

The use of differentiable physics for planning and policy learning has been explored, with one body of work using differentiable simulators with backpropagation through time to compute deterministic policy gradients [37, 45, 57, 13]. However, these methods suffer from exploding or vanishing gradients, limiting their scalability and stability over long horizons.

Differentiable simulators have also been applied to trajectory optimization, where gradients of the system dynamics are used to iteratively refine trajectories [20, 27, 22]. In these methods, contact smoothing is typically present but not introduced deliberately; rather, it emerges implicitly because contact dynamics are commonly formulated as linear complementarity programs (LCPs) and can only be solved approximately [19, 56], effectively smoothing contact interactions. Consequently, these approaches are often restricted to locomotion tasks, where gravity naturally enables the robot to reestablish contact after contact is broken, or to scenarios where optimization is performed within a fixed contact mode [25].

Other works explicitly optimize trajectories and contact forces jointly [33, 6, 38, 7] and require enforcing complementarity constraints between contact forces and signed distances. Complementarity-based formulations are generally NP-hard, and in practice, even with approximate solvers, they often still require specifying contact modes and sequences.

Across all these methods, the resulting optimization problems are prone to local minima. For global contact-rich planning, methods based on the rapidly exploring random tree (RRT) [42], mixed integer programming (MIP) [17], and the graph of convex sets (GCS) [34, 15] have been proposed. While these methods can perform global search, they are typically limited to low-dimensional systems and are vulnerable to combinatorial explosion of the number of contact modes.

III. PRELIMINARIES AND PROBLEM STATEMENT

Conic Programs Throughout this paper, we make extensive use of convex conic programs of the form

$$\begin{aligned} & \underset{x,s}{\text{minimize}} \quad \frac{1}{2} x^\top P x + q^\top x \\ & \text{subject to} \quad Ax + s = b, \quad s \in \mathcal{K}, \end{aligned} \tag{1}$$

where \mathcal{K} is a Cartesian product of symmetric cones, i.e., $\mathcal{K} = \mathcal{K}_1 \times \mathcal{K}_2 \times \dots \times \mathcal{K}_I$. Each \mathcal{K}_i is either a non-negative cone or a second-order cone. A variety of numerical solvers can be used to solve (1), including [14].

The Karush-Kuhn-Tucker (KKT) conditions of (1) are

$$Px + q + A^\top z = 0 \tag{2a} \quad s \circ z = \kappa e \tag{2c}$$

$$Ax + s - b = 0 \tag{2b} \quad s \in \mathcal{K}, z \in \mathcal{K}^* \tag{2d}$$

where $\kappa = 0$, \mathcal{K}^* denotes the dual cone of \mathcal{K} , and the product $s \circ z$ is defined blockwise as $(s \circ z)_i = s_i \circ z_i$. For each block,

$$u \circ v = \begin{cases} [u_1 v_1 \dots u_p v_p]^\top & \text{if } \mathcal{K}_i \text{ is a non-negative cone,} \\ [u^\top v \quad u_0 v_1^\top + v_0 u_1^\top]^\top & \text{if } \mathcal{K}_i \text{ is a second-order cone.} \end{cases}$$

The vector $e = [e_1^\top \ \cdots \ e_I^\top]^\top$ is given by

$$e_i = \begin{cases} [1 \ 1 \ \cdots \ 1]^\top & \text{if } \mathcal{K}_i \text{ is a non-negative cone,} \\ [1 \ 0 \ \cdots \ 0]^\top & \text{if } \mathcal{K}_i \text{ is a second-order cone.} \end{cases}$$

Relaxing the complementarity condition (2c) by allowing $\kappa > 0$ yields the KKT conditions of the following convex barrier-penalized problem:

$$\begin{aligned} & \underset{x, s}{\text{minimize}} \quad \frac{1}{2}x^\top Px + q^\top x + \kappa \sum_{i=1}^I \psi_i(s_i) \\ & \text{subject to} \quad Ax + s = b, \end{aligned} \quad (3)$$

where $\psi_i(\cdot)$ is the logarithmic barrier associated with \mathcal{K}_i ,

$$\psi_i(u) = \begin{cases} -\sum_{j=1}^p \log(u_j) & \text{if } \mathcal{K}_i \text{ is a non-negative cone,} \\ -\frac{1}{2} \log(u_0^2 - u_1^\top u_1) & \text{if } \mathcal{K}_i \text{ is a second-order cone.} \end{cases}$$

Details on the equivalence between complementarity relaxation and logarithmic barriers are given in [9, §11.2] and [55].

Contact Models We adopt the quasidynamic model of contact dynamics from [41, 42]. This model assumes that velocities are sufficiently small to be neglected, and employs a convex formulation of contact dynamics [5], thereby avoiding the need to solve LCPs. A key advantage of this assumption is that it reduces the number of state variables by half, significantly simplifying the trajectory optimization problem. This assumption is well suited for manipulation tasks in which departures from static equilibrium are brief, so that transient accelerations do not integrate into significant velocities [35, §10.1].

In this setting, the true hybrid dynamics $f_0 : \mathcal{X} \times \mathcal{U} \rightarrow \mathcal{X}$ from the current state and input to the next state $(x, u) \mapsto x^+$ is defined implicitly as the argmin of the conic program:

$$\begin{aligned} & \underset{x^+, \nu}{\text{minimize}} \quad \frac{1}{2}(x^+)^\top P(x) x^+ + q(x, u)^\top x^+ \\ & \text{subject to} \quad \nu_i = J_i(x)(x^+ - x) + [\phi_i(x) \ 0 \ 0]^\top, \quad (4) \\ & \nu_i \in \mathcal{F}_i^*, \quad \forall i = 1, \dots, n_c, \end{aligned}$$

where n_c denotes the number of contact pairs. Additional details of the model are in Appendix B. We can write the κ -smoothed dynamics $f_\kappa : \mathcal{X} \times \mathcal{U} \rightarrow \mathcal{X}$ as the argmin of (5):

$$\begin{aligned} & \underset{x^+, \nu}{\text{minimize}} \quad \frac{1}{2}(x^+)^\top P(x) x^+ + q(x, u)^\top x^+ + \kappa \sum_{i=1}^I \psi_i(\nu_i) \\ & \text{subject to} \quad \nu_i = J_i(x)(x^+ - x) + [\phi_i(x) \ 0 \ 0]^\top, \quad (5) \\ & \quad \forall i = 1, \dots, n_c, \end{aligned}$$

the same as how (1) is relaxed to (3). In addition to the primal solution of (4) or (5), which yields the next state x^+ , the dual variables λ_i represent contact forces.

Problem Statement We aim to 1) build a reachability-friendly differentiable simulator, 2) bound smoothing error for reachability, and 3) use it for certified contact-rich planning.

Problem 1: Efficient differentiable simulator based on convex optimization. Build a fast differentiable simulator that avoids solving LCPs while enabling fast, accurate gradient queries for planning. The simulator must provide gradients of positions x and contact forces λ with respect to smoothing parameter κ .

Problem 2: Reachability for contact-rich dynamics. Find a tight, efficiently computable, and differentiable bound on the smoothing error $\|f_\kappa(x, u) - f_0(x, u)\|$, and propagate it through (4) to obtain reachable state/control tubes $\{\mathcal{R}_k^x\}_{k=0}^N$ and $\{\mathcal{R}_k^u\}_{k=0}^{N-1}$. These tubes must guarantee that the *true* executed trajectory satisfies $x_k \in \mathcal{R}_k^x \subseteq \mathcal{X}$ and $u_k \in \mathcal{R}_k^u \subseteq \mathcal{U}$ for all k , where (x_k, u_k) evolves under the *hybrid* dynamics (4).

Problem 3: Robust feedback motion planning for smoothed contact dynamics. Optimize a nominal state $\mathbf{z} := \{(z_i)\}_{i=0}^N$ and control $\mathbf{v} := \{(v_i)\}_{i=0}^{N-1}$ trajectory that is feasible under the κ -smoothed dynamics (5) and a causal feedback controller $\pi := (\pi_0, \dots, \pi_{N-1})$, where $\pi_i : (\mathbb{R}^{n_x})^{i+1} \rightarrow \mathbb{R}^{n_u}$, that stabilizes the true hybrid dynamics (4) about (\mathbf{z}, \mathbf{v}) and ensures closed-loop satisfaction of state and control constraints.

Outline Next, we will present our differentiable simulator and smoothing error bound (Sec. IV) and our reachability-certified contact-rich feedback motion planner (Sec. V).

IV. DIFFERENTIABLE SIMULATOR WITH CONTACT SMOOTHING BOUNDS

A. Differentiable Simulator

Convex conic programs of the form (1) or (3) can be embedded as differentiable layers within computational graphs [1, 3]. When P , q , A , and b depend on problem data θ , the sensitivity of the solution x and s with respect to θ can be computed [2]. The sensitivity of the solution with respect to the complementarity value κ can also be computed. The corresponding implicit differentiation formulas are summarized in Appendix A.

Utilizing the ability to differentiate through convex conic programs, we can differentiate the dynamics $(x, u) \mapsto x_\kappa^+$ implicitly defined by (5) to obtain $\partial x_\kappa^+ / \partial x$ and $\partial x_\kappa^+ / \partial u$. We can also compute the sensitivity with respect to κ , which is required for the smoothing deviation bound, as derived next.

B. Smoothing of Contact Dynamics

The smoothing of the true hybrid dynamics $x^+ = f_0(x, u)$, defined implicitly by (4), into the smoothed dynamics $x_\kappa^+ = f_\kappa(x, u)$, defined by (5) via complementarity relaxation, is necessitated by the inherent nonsmoothness of the former. When the complementarity value is zero, the dynamics are piecewise defined: if the signed distance is strictly positive, the corresponding contact force vanishes and the object state x_o^+ is independent of the control input u ; if the signed distance is zero, contact is active and u influences x_o^+ through the induced contact forces. Consequently, the mapping $(x, u) \mapsto x^+$ is locally constant with respect to u in regions without contact and switches abruptly to a different regime when contact is established. This discontinuous change in the active constraints gives rise to kinks and flat regions in f_0 , rendering it nonsmooth.

In contrast, complementarity relaxation permits the contact force to vary smoothly as a function of the signed distance, yielding a smooth mapping $(x, u) \mapsto x_\kappa^+$. This removes the sharp switching between inactive and active contact modes that characterizes the true dynamics.

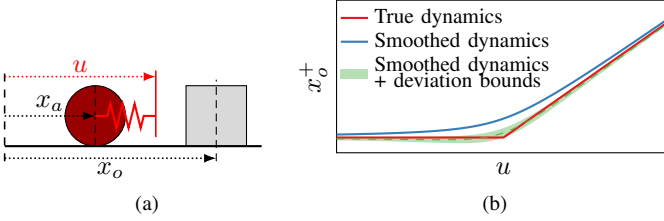


Figure 2. 1D pusher. (a) System schematic. (b) Discrete-time dynamics $x^+ = f(x, u)$, with x_o^+ plotted versus the input u .

Relaxing the complementarity condition, however, inevitably introduces a discrepancy between the true and smoothed dynamics. Although this discrepancy may be small over a single timestep, it can accumulate over time and result in significant deviations. This creates a fundamental tension: the smoothed dynamics are essential for obtaining informative gradients, yet our ultimate objective is to provide guarantees with respect to the true hybrid dynamics. To address this issue, we first quantify the discrepancy between the true and smoothed dynamics, as formalized in the following theorem.

Theorem 1. The true dynamics $x^+ = f_0(x, u)$ and the smoothed dynamics $x_\kappa^+ = f_\kappa(x, u)$ satisfy

$$f_0(x, u) = f_\kappa(x, u) - P(x)^{-1} \sum_{i=1}^{n_c} J_i(x)^\top \frac{\partial \lambda_{\kappa, i}}{\partial \kappa} \kappa w_i, \quad (6)$$

where $\lambda_{\kappa, i}$ is the i th contact force under the smoothed dynamics and $w_i \in [1, 2]$, under the assumption that $J_i P^{-1} J_j^\top = 0$ for all $i \neq j$. Moreover, the bound is tight in the sense that for every $w_i \in \{1, 2\}$, there exist (x, u) pairs that satisfy (6).

The proof of Theorem 1 is provided in Appendix C. Equation (6) can be written compactly as

$$x^+ = f_\kappa(x, u) + E_\kappa(x, u) w, \quad (7)$$

where $w \in [1, 2]^{n_c}$ and the i th column of E_κ is given by

$$E_{\kappa, i} = -P(x)^{-1} J_i(x)^\top \frac{\partial \lambda_{\kappa, i}}{\partial \kappa} \kappa.$$

Both f_κ and E_κ are everywhere differentiable. The intuition behind this set-valued discrepancy is best shown via example.

Example 1. Consider the 1D system of a stiffness-controlled red pusher pushing a gray object, shown schematically in Fig. 2a. The corresponding discrete-time dynamics are plotted in Fig. 2b. Under the true dynamics, when the pusher is not in contact with the object, the object position remains constant with respect to the input, resulting in flat regions and nonsmooth transitions between the non-contact and contact modes.

By smoothing the dynamics, the gradient $\partial x_o^+ / \partial u$ becomes positive for all values of u . These gradients are informative, as they guide the optimizer toward actions that induce contact, and they remain continuous across the entire input domain. The shaded region in Fig. 2b represents the bounds induced by the smoothing error: its upper and lower envelopes correspond to $f_\kappa(x, u) + E_\kappa(x, u)$ and $f_\kappa(x, u) + 2E_\kappa(x, u)$, respectively. As predicted by (7), the true dynamics lie entirely within this shaded region.

One may also ask if the nominal dynamics could instead be chosen as $f_\kappa(x, u) + 1.5E_\kappa(x, u)$, shown as the dashed line in Fig. 2b, to eliminate the bias. The answer is no. Such a choice yields zero or even negative $\partial x_o^+ / \partial u$ gradients over parts of the input domain, rendering them non-informative for action refinement. In contrast, using $f_\kappa(x, u)$ as the nominal dynamics preserves informative gradients, while the one-sided uncertainty term $E_\kappa(x, u) w$ accounts for the discrepancy between the κ -smoothed dynamics and the true hybrid dynamics.

Remark 1. The assumption in Theorem 1 that $J_i P^{-1} J_j^\top = 0$ for all $i \neq j$ is made for analytical convenience. In practice, (6) holds for sufficiently large values of $M_o / \delta t^2$. Moreover, we empirically observe that the bounds yield correct tube-valued predictions, even under multicontact scenarios (Section VI).

C. Smoothing of Contact Geometry

The complementarity between signed distance and contact force is not the only source of nonsmoothness in the mapping $(x, u) \mapsto x^+$. The geometry of contact primitives can also introduce nonsmoothness. For example, in contact between a sphere and a polyhedron, nonsmoothness arises from discontinuous changes in surface normals across the faces of the polyhedron. This results in discontinuities in the contact Jacobian and, consequently, in a nonsmooth dynamics mapping $(x, u) \mapsto x^+$. This issue has also been identified in prior work [36, 26].

In this work, we utilize the differentiability of conic programs by formulating contact point queries as quadratic programs (QPs). For instance, the contact points between a sphere $\{p_1 \mid \|p_1 - p_c\|_2 \leq r\}$ and a polyhedron $\{p_2 \mid A p_2 \leq b\}$ are obtained by solving a relaxed version of the QP

$$\text{minimize } \frac{1}{2} \|p_2 - p_c\|_2^2 \quad \text{subject to } A p_2 \leq b,$$

analogous to how (1) is relaxed to (3). The resulting contact points are then used to compute the contact Jacobian $J_i(x)$ and signed distance $\phi_i(x)$, which enter into (4).

Ideally, one would characterize how such geometric smoothing induces deviations in the contact Jacobian and signed distance, and thus in the dynamics mapping $(x, u) \mapsto x^+$. We defer this analysis to future work, as the error introduced by geometric smoothing is less severe than that arising from contact dynamics smoothing. In particular, contact dynamics smoothing introduces a force-at-a-distance effect whose error can accumulate over time, whereas geometric smoothing primarily induces a local perturbation that manifests as a constant offset.

V. TRAJECTORY OPTIMIZATION AND POLICY SYNTHESIS

We aim to solve the trajectory optimization problem:

$$\text{minimize } J(\mathbf{z}, \mathbf{v}) \quad (8a)$$

$$\text{subject to } z_{k+1} = f_\kappa(z_k, v_k), \quad \forall k = 0, \dots, N-1, \quad (8b)$$

$$z_0 = x_0, \quad (8c)$$

where $\mathbf{z} = [z_0^\top \dots z_N^\top]^\top$ is the nominal state trajectory and $\mathbf{v} = [v_0^\top \dots v_{N-1}^\top]^\top$ is the nominal control sequence. The cost $J(\mathbf{z}, \mathbf{v})$ may include terms such as

$\sum_{k=0}^N \frac{1}{2} \|z_k - x_{\text{goal}}\|_Q^2$. The dynamics constraint (8b) is based on the smoothed dynamics f_κ rather than the true hybrid dynamics f_0 . This choice is necessary because f_0 does not provide informative gradients: its associated optimization landscape contains flat regions and sharp discontinuities that hinder gradient-based optimization.

However, when executing the nominal control sequence \mathbf{v} on the true hybrid dynamics, the resulting state trajectory $\mathbf{x} = [x_0^\top \dots x_N^\top]^\top$ deviates from \mathbf{z} . As a consequence, there is no guarantee that \mathbf{x} will reach the goal state x_{goal} . More critically, in the presence of state or control constraints, the true trajectory may violate constraints even if the nominal trajectory is feasible. These issues persist even under repeated replanning of (8) in a model predictive control (MPC) fashion, as the mismatch between the smoothed and true dynamics is not explicitly accounted for. The key idea is that, instead of executing the nominal control on the true hybrid dynamics, we execute a *policy*. Specifically, consider a class of affine feedback policies that has the form

$$u_k = \pi(x_0, \dots, x_k) = v_k + \sum_{j=0}^k K_{kj} (x_j - z_j), \quad (9)$$

where K_{kj} are the feedback gains. By using such a policy, we can analytically compute tube-valued predictions of the closed-loop behavior of the true hybrid dynamics. This result is formalized in the following theorem.

Theorem 2. For the true dynamics (7), consider strictly lower-triangular block matrices

$$\Phi^x = \begin{bmatrix} 0 & & & \\ \Phi_{1,0}^x & & & \\ \vdots & \ddots & & \\ \Phi_{N,0}^x & \dots & \Phi_{N,N-1}^x & \end{bmatrix}, \Phi^u = \begin{bmatrix} 0 & & & \\ \Phi_{1,0}^u & & & \\ \vdots & & \ddots & \\ \Phi_{N-1,0}^u & \dots & \Phi_{N-1,N-2}^u & 0 \end{bmatrix},$$

that satisfy, for all $j = 0, \dots, N-1$,

$$\begin{aligned} \Phi_{k+1,j}^x &= A_k \Phi_{k,j}^x + B_k \Phi_{k,j}^u, \quad \forall k = j+1, \dots, N-1, \\ \Phi_{j+1,j}^x &= E_j, \end{aligned}$$

where $A_k = \partial f_\kappa(z_k, v_k)/\partial z$, $B_k = \partial f_\kappa(z_k, v_k)/\partial v$, and $E_j = E_\kappa(z_j, v_j)$. The set of all such block matrices Φ^x and Φ^u parameterize all possible closed-loop system responses

$$\mathbf{x} = \mathbf{z} + \Phi^x \mathbf{w} \quad \text{or} \quad x_k = z_k + \sum_{j=0}^{k-1} \Phi_{k,j}^x w, \quad (10a)$$

$$\mathbf{u} = \mathbf{v} + \Phi^u \mathbf{w} \quad \text{or} \quad u_k = v_k + \sum_{j=0}^{k-1} \Phi_{k,j}^u w, \quad (10b)$$

with $\mathbf{w} \in [1, 2]^{N \times n_c}$. Moreover, a feedback policy of the form

$$\mathbf{u} = \mathbf{v} + \Phi^u(\Phi^x)^{-1}(\mathbf{x} - \mathbf{z}) := \mathbf{v} + \mathbf{K}(\mathbf{x} - \mathbf{z})$$

achieves such a closed-loop response.

The proof of Theorem 2 is provided in Appendix D. By leveraging Theorem 2, we can formulate an optimization problem in which the closed-loop response is guaranteed to satisfy the stage and terminal constraints

$$G_k \begin{bmatrix} x_k \\ u_k \end{bmatrix} + g_k \leq 0, \quad \forall k = 0, \dots, N-1, \quad (11a)$$

$$G_f x_N + g_f \leq 0. \quad (11b)$$

The optimization problem that jointly optimizes the nominal trajectory and affine feedback policy is formulated as

$$\min_{\substack{\mathbf{z}, \mathbf{v}, \\ \Phi^x, \Phi^u}} J(\mathbf{z}, \mathbf{v}) + \mathcal{J}(\Phi^x, \Phi^u) \quad (12a)$$

$$\text{s.t.} \quad z_{k+1} = f_\kappa(z_k, v_k), \quad z_0 = x_0, \quad (12b)$$

$$\Phi_{k+1,j}^x = A_k \Phi_{k,j}^x + B_k \Phi_{k,j}^u, \quad \Phi_{j+1,j}^x = E_j, \quad (12c)$$

$$\underbrace{\sum_{j=0}^{k-1} G_k \begin{bmatrix} \Phi_{k,j}^x \\ \Phi_{k,j}^u \end{bmatrix} w_c + w_r \|G_k \begin{bmatrix} \Phi_{k,j}^x \\ \Phi_{k,j}^u \end{bmatrix}\|_{\text{row},q}}_{h_k(\Phi^x, \Phi^u)} + G_k \begin{bmatrix} z_k \\ v_k \end{bmatrix} + g_k \leq 0, \quad (12d)$$

$$\underbrace{\sum_{j=0}^{N-1} G_f \Phi_{N,j}^x w_c + w_r \|G_f \Phi_{N,j}^x\|_{\text{row},q}}_{h_f(\Phi^x)} + G_f z_N + g_f \leq 0, \quad (12e)$$

where $\|\cdot\|_{\text{row},q}$ denotes the row-wise q -norm. The constraints (12d) and (12e) correspond to the stage constraint (11a) and the terminal constraint (11b), respectively. Their form follows from the closed-loop system response representation in (10) and a standard robustification argument. Specifically, recall

$$w \in [1, 2]^{n_c} = \{w \in \mathbb{R}^{n_c} \mid \|w - w_c\|_p \leq w_r\},$$

where $w_c = 1.5 \mathbf{1}$, $w_r = 0.5$, and $p = \infty$. For any vector $a \in \mathbb{R}^{n_c}$, the worst-case value of the linear function $a^\top w$ over this uncertainty set admits the closed-form expression

$$\max_{w \in [1, 2]^{n_c}} a^\top w = a^\top w_c + w_r \|a\|_q,$$

where q is the dual norm exponent satisfying $1/p + 1/q = 1$. Applying this property row-wise to the affine dependence of (x_k, u_k) on w in (10) yields the robust constraints in (12).

We do not explicitly account for model mismatch introduced by estimating the nonlinear tracking error dynamics as a linear time-varying (LTV) system. This can be addressed via linearization error bounds [29] computed via interval arithmetic [31] or statistical methods [24, 23], which inflate the tubes to maintain guarantees.

A. Cost and Constraints

The cost (12a) includes two components:

- Nominal trajectory cost, encouraging goal reaching and smooth controls.

$$J(\mathbf{v}, \mathbf{z}) = \sum_{k=0}^N \frac{1}{2} \|z_k - x_{\text{goal}}\|_Q^2 + \sum_{k=0}^{N-2} \frac{1}{2} \|v_k - v_{k+1}\|_R^2.$$

- Tube cost, which penalizes the size of the tube.

$$\mathcal{J}(\Phi^x, \Phi^u) = \sum_{j=0}^{N-1} \left(\sum_{k=j+1}^N \|\bar{Q}^{\frac{1}{2}} \Phi_{k,j}^x\|_{\mathcal{F}}^2 + \sum_{k=j+1}^{N-1} \|\bar{R}^{\frac{1}{2}} \Phi_{k,j}^u\|_{\mathcal{F}}^2 \right),$$

The constraints (12d) and (12e), or equivalently (11), enforce the following:

- Joint angle and torque limits.

- Non-collision constraints, locally approximated by affine inequalities.
- Object position constraints, which require the object state to lie within a polytopic set.

B. Solver Algorithm

We solve the optimization problem (12) using a sequential convex programming (SCP) approach. At each iteration, we linearize around the current nominal trajectory (\mathbf{z}, \mathbf{v}) and solve the resulting convex optimization problem:

$$\min_{\delta\mathbf{z}, \delta\mathbf{v}, \Phi^x, \Phi^u} J(\mathbf{z} + \delta\mathbf{z}, \mathbf{v} + \delta\mathbf{v}) + \mathcal{J}(\Phi^x, \Phi^u) \quad (13a)$$

$$\text{s.t. } \delta z_{k+1} = A_k \delta z_k + B_k \delta v_k, \quad \delta z_0 = 0, \quad (13b)$$

$$\begin{aligned} \Phi_{k+1,j}^x &= A_k \Phi_{k,j}^x + B_k \Phi_{k,j}^u, \\ \Phi_{j+1,j}^x &= E_j + \frac{\partial E_j}{\partial z} \delta z_j + \frac{\partial E_j}{\partial v} \delta v_j, \end{aligned} \quad (13c)$$

$$h_k(\Phi^x, \Phi^u) + G_k \begin{bmatrix} z_k + \delta z_k \\ v_k + \delta v_k \end{bmatrix} + g_k \leq 0, \quad (13d)$$

$$h_f(\Phi^x) + G_f(z_N + \delta z_N) + g_f \leq 0, \quad (13e)$$

$$\|\delta\mathbf{z}\| \leq \varepsilon, \quad \|\delta\mathbf{v}\| \leq \varepsilon. \quad (13f)$$

The constraints (13f) ensure the validity of the local linearization. The resulting increments $\delta\mathbf{z}$ and $\delta\mathbf{v}$ are then used to update the nominal trajectory, and the procedure is repeated until convergence. The full algorithm is summarized below.

Algorithm 1: Certifiable Gradient-Based Policy Synthesis

```

Input: Initial control sequence  $\mathbf{v}$ , initial state  $x_0$ 
Output: Nominal trajectory  $(\mathbf{z}, \mathbf{v})$ , feedback gains  $\mathbf{K}$ 
// SCP iterations
1 for  $iter = 1$  to  $maxIters$  do
2    $z_0 \leftarrow x_0$ 
3   for  $k = 0$  to  $N - 1$  do
4      $| z_{k+1} \leftarrow f_\kappa(z_k, v_k)$ 
5   end
6    $\mathbf{A}, \mathbf{B} \leftarrow \text{LinearizeDynamics}(f_\kappa, \mathbf{z}, \mathbf{v})$ 
7    $\mathbf{E}, \frac{\partial \mathbf{E}}{\partial \mathbf{z}}, \frac{\partial \mathbf{E}}{\partial \mathbf{v}} \leftarrow \text{EvaluateDisturbance}(E_\kappa, \mathbf{z}, \mathbf{v})$ 
8    $\delta\mathbf{z}, \delta\mathbf{v}, \Phi^x, \Phi^u \leftarrow \text{Solve}(13)(\mathbf{z}, \mathbf{v}, \mathbf{A}, \mathbf{B}, \mathbf{E}, \frac{\partial \mathbf{E}}{\partial \mathbf{z}}, \frac{\partial \mathbf{E}}{\partial \mathbf{v}})$ 
9    $\mathbf{v} \leftarrow \mathbf{v} + \delta\mathbf{v}$ 
10 end
// Post-processing
11  $\mathbf{K} \leftarrow \Phi^u(\Phi^x)^{-1}$ 
12 for  $k = 0$  to  $N - 1$  do
13    $| v_k \leftarrow v_k + \sum_{j=0}^k K_{kj} (x_j - z_j)$ 
14    $| z_{k+1} \leftarrow f_\kappa(z_k, v_k)$ 
15    $| x_{k+1} \leftarrow f_0(x_k, v_k)$ 
16 end
17 return  $\mathbf{z}, \mathbf{v}, \mathbf{K}$ 

```

While the optimization problem (13) is convex and can be solved by standard solvers, its structure can be exploited to drastically improve computational efficiency. A specialized solver is detailed in Appendix E.

C. Baseline

We compare our method against a baseline approach trajectory optimization with contact trust region (TO-CTR) pro-

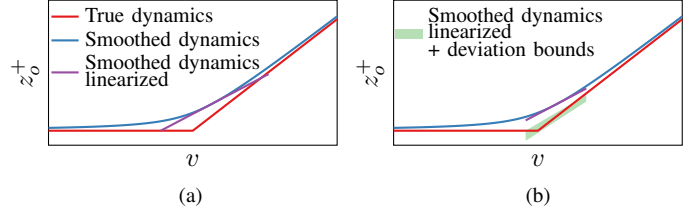


Figure 3. Linearization of the smoothed dynamics $z^+ = f_\kappa(z, v)$ for a 1D pusher as viewed by (a) TO-CTR and (b) our method.

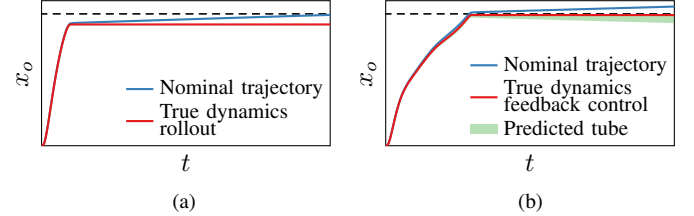


Figure 4. Rollouts of the 1D pusher system for pushing the object to reach a goal position (dashed line) using (a) TO-CTR and (b) our method.

posed in [51]. The method is closely related to iterative linear quadratic regulator (iLQR), but augments the backward pass with a heuristic CTR constraint. Specifically, during the backward pass, instead of solving (13), TO-CTR solves the following convex optimization problem:

$$\min_{\delta\mathbf{z}, \delta\mathbf{v}} J(\mathbf{z} + \delta\mathbf{z}, \mathbf{v} + \delta\mathbf{v}) \quad (14a)$$

$$\text{s.t. } \delta z_{k+1} = A_k \delta z_k + B_k \delta v_k, \quad \delta z_0 = 0, \quad (14b)$$

$$G_k \begin{bmatrix} z_k + \delta z_k \\ v_k + \delta v_k \end{bmatrix} + g_k \leq 0, \quad (14c)$$

$$G_f(z_N + \delta z_N) + g_f \leq 0, \quad (14d)$$

$$\|\delta\mathbf{z}\| \leq \varepsilon, \quad \|\delta\mathbf{v}\| \leq \varepsilon, \quad (14e)$$

$$\lambda_\kappa + \frac{\partial \lambda_\kappa}{\partial z_k} \delta z_k + \frac{\partial \lambda_\kappa}{\partial v_k} \delta v_k \in \mathcal{F}. \quad (14f)$$

The constraint (14f) enforces the CTR by restricting the linearized contact force to remain within the friction cone \mathcal{F} . An intuitive explanation of the key difference between TO-CTR and our method is best illustrated through an example.

Example 2. We consider a 1D stiffness-controlled pusher-object system (Fig. 2a). The linearized dynamics used by TO-CTR and our method are shown in Fig. 3a and Fig. 3b. TO-CTR assumes that the linearization of the smoothed dynamics accurately approximates the true hybrid dynamics over control perturbations δv satisfying the CTR constraint $\lambda_\kappa + \frac{\partial \lambda_\kappa}{\partial v} \delta v \geq 0$ and $|\delta v| \leq \varepsilon$. As illustrated, this approximation error remains non-negligible within the assumed region. In contrast, our method explicitly bounds the discrepancy between the smoothed and true hybrid dynamics, guaranteeing that for all $|\delta v| \leq \varepsilon'$, the true dynamics lies within a known deviation of the smoothed model.

This difference is evident in the rollouts Fig. 4. TO-CTR exploits a force-at-a-distance artifact of the smoothed dynamics to reach the goal, but fails when executed on the true dynamics (Fig. 4a). Our method compensates for this discrepancy during optimization, yielding better goal attainment in closed loop, with rollouts remaining within the predicted tube (Fig. 4b).

TABLE I
TASK PARAMETERS

	Time step size (s)	Time steps	Dynamics smoothing	Geometry smoothing
Bimanual Planar Bucket	0.02	100	10^{-3}	0
Bimanual Planar Box	0.02	100	10^{-3}	10^{-3}
In-hand cube	0.02	50	10^{-4}	0

VI. EXPERIMENT RESULTS AND DISCUSSION

Through a series of simulated and real-world experiments, we seek to answer the following research questions (RQs):

- RQ1.** Do closed-loop rollouts of the true hybrid dynamics remain within the predicted tube?
- RQ2.** Does our method achieve lower goal-reaching error than the baseline while strictly enforcing constraints?
- RQ3.** Does performance degrade due to strict constraint enforcement?
- RQ4.** Is contact geometry smoothing necessary in practice?
- RQ5.** Can our method scale to high-dimensional systems?

Parameters for the experimented tasks are listed in Table I. We perform all computations on a desktop computer with an Intel Core Ultra 9 285K processor and 64 GB RAM.

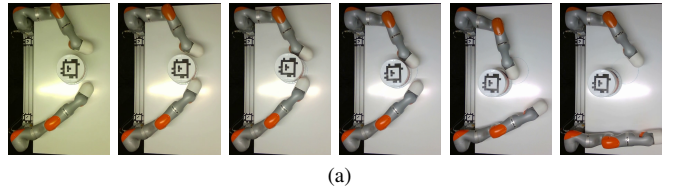
A. Bimanual Planar Bucket Manipulation

Regarding the choice of smoothing parameter, values that are too small yield near-zero gradients, while larger values increase the tube size. Empirically, we found $\kappa = 10^{-3}$ to balance gradient informativeness and tube size.

First, we evaluate on bimanual hardware, with two Kuka iiwa 7 arms each acting as a 3DoF finger (Fig. 5). The goal is to rotate and translate the bucket to a desired goal location. We note that in spite of sim-to-real modeling errors and apart from noise from position estimates, the bucket stays largely within the computed tubes, affirming **RQ1**; strict containment could be achieved by inflating $E_\kappa(x, u)$ with a bound reflecting the perception noise [11].

We also use this setting to compare with the baseline (Sec. V-C). We sampled a set of initial and target states and computed a trajectory or policy using both the baseline and our method. Any samples deemed infeasible by either algorithm were discarded. A quantitative comparison between our method and the baseline is presented in Table II. All reported metrics are averaged over 1000 experiments. We also provide distributions of the realized goal errors in Appendix F.

We compare performance against the baseline both with and without replanning. Without replanning, our method achieves lower average goal position and orientation error than the baseline. When using MPC, the difference becomes negligible. Therefore, we confirm **RQ2**: our method improves goal-reaching accuracy, although the improvement is modest. This is because the planning horizon is not long enough for smoothing errors to accumulate sufficiently to invalidate the TO-CTR trajectory. Importantly, our method strictly enforces constraints. In contrast, although the nominal TO-CTR trajectory is feasible, it is not guaranteed to remain feasible when executed on the true system dynamics. Constraint-violating failure modes are illustrated in Appendix F.



(a)

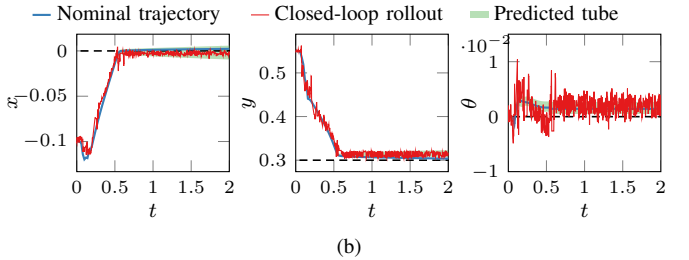


Figure 5. Rollout of bimanual planar bucket manipulation. (a) Time-lapse. (b) Rollout and predicted tube.

TABLE II
COMPARISON OF ALGORITHMS ON BIMANUAL PLANAR BUCKET MANIPULATION

	TO-CTR	Ours	TO-CTR with MPC	Ours with MPC
MPC horizon	-	-	1	1
Goal position error (m)	0.1522	0.1447	0.1558	0.1538
Goal angle error (rad)	0.1034	0.0946	0.0985	0.0987
Nominal trajectory cost	313.51	299.43	-	-
Constraint violating rollouts	3.1%	0.0%	1.2%	0.0%
Execution time (s)	88.2	85.9	6.36	6.99

We also address **RQ3**. Strict constraint enforcement does not degrade performance. In fact, our method achieves lower evaluated cost $J(\mathbf{z}, \mathbf{v})$, requiring smaller control effort and incurring lower state cost than the baseline. This suggests that the tube-based reasoning enables the optimizer to select contacts less conservatively. In contrast, the baseline's CTR condition appears overly conservative relative to the tube characterization, prematurely marking certain transitions as infeasible. Our method further improves robust constraint satisfaction. Because the baseline does not account for smoothing error, it incurs self-collisions under the true hybrid dynamics, which can damage the manipulator. Re-planning via MPC also does not eliminate these violations. In contrast, our approach reasons directly about reachable tubes, guaranteeing safety in both open- and closed-loop execution.

Overall, this experiment validates **RQ1–RQ3**. Closed-loop executions of the true hybrid dynamics remain within the predicted tubes (RQ1). We obtain modest improvements in goal-reaching error without sacrificing performance (RQ2–RQ3), while providing a formal certificate of robust constraint satisfaction (RQ1).

B. Bimanual Planar Box Manipulation

Next, we evaluate our method on a planar box manipulation problem to motivate the need for geometry smoothing (RQ4). In this setting, the discontinuous gradients that arise between the actuated arms and the non-smooth normals from the box destabilize the method without geometry smoothing (Fig. 6a,c). While the closed-loop rollout remains within the reachable tube, once again validating **RQ1**, the box fails to approach the target, leading to a final goal error of 54 cm,

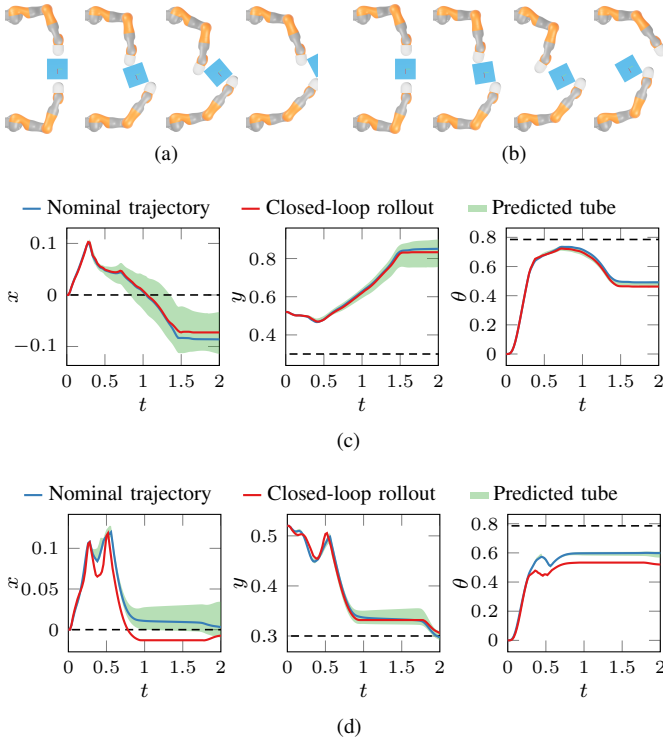


Figure 6. Rollout of bimanual planar box manipulation. Keyframes under (a) non geometry smoothing, and (b) has geometry smoothing. Trajectory and predicted tube per object DoF under (c) non geometry smoothing, and (d) has geometry smoothing.

which is in fact further from the goal than the initial state, due to the unstable gradients. In contrast, with geometry smoothing, we find a solution that gets much closer to the target, leading to a goal error of 9 mm. In this case, the closed-loop rollouts do not stay within the reachable tubes, as those discrepancies are not accounted for in the bound $E_\kappa(x, u)$. However, as noted earlier, the resulting error only leads to a small constant offset from the tubes for some states, while getting closer to the goal. Overall, this result demonstrates the need for geometry smoothing for manipulating objects with discontinuous surface normals, validating **RQ4**, though this is at the cost of tube validity (**RQ1**).

C. In-hand Cube Reorientation

Finally, we evaluate our method on a high-dimensional dexterous in-hand manipulation task using an Allegro hand manipulating a cube. The system consists of 16 actuated degrees of freedom and 6 unactuated object degrees of freedom. The objective is to rotate the cube by 90° (i.e., achieve a roll angle of $\pi/2$) while maintaining its center of mass position and the remaining Euler angles. This yields a 22-dimensional state and 16-dimensional control input system, providing a challenging test of scalability (**RQ5**). Despite the high dimensionality and contact-rich dynamics, Alg. 1 synthesizes the solution shown in Fig. 1 in 610.3 seconds. We again validate **RQ1**: the true closed-loop trajectory remains within the predicted reachable tubes. Although the tube size grows due to the smoothing error and contact transitions, the closed-loop post-processing step in Alg. 1 ensures accurate

goal convergence. The resulting goal error is 8 mm and 1.2° . Overall, this experiment demonstrates that Alg. 1 scales to high-dimensional, complex, contact-rich manipulation tasks while retaining a reachability-based certificate that guarantees robust constraint satisfaction.

VII. LIMITATIONS

Despite enabling gradient-based policy synthesis for contact-rich manipulation with formal guarantees on the true hybrid dynamics, our framework has several limitations. First, although the set-valued deviation is globally valid, the SCP solver relies on local linearizations. It remains unclear when this approximation becomes insufficient and whether local quadratic approximations, such as those used in differential dynamic programming (DDP), are necessary. Second, we account only for errors induced by contact smoothing, and do not model uncertainty in physical parameters such as mass, friction, or geometry. Extending the framework to incorporate parametric uncertainty is an important direction for future work. Third, our formulation relies on a quasidynamic model and assumes contact only between actuated and unactuated bodies, and thus does not extend to dynamic manipulation or tool-use scenarios. Finally, like most optimization-based methods, the synthesized policy converges to a local optimum and produces only local manipulation behaviors. In contrast, while policy-gradient RL methods also converge to local optima, their policy parameterization combined with stochastic exploration can yield more global manipulation strategies.

VIII. CONCLUSION

We presented a principled framework for handling hybrid dynamics that overcomes the nonsmoothness which has traditionally plagued gradient-based trajectory optimization, while retaining certifiable guarantees on closed-loop behavior.

The key ingredients are as follows. First, we smooth the hybrid dynamics to eliminate discontinuities and zero gradients that hinder optimization; for contact dynamics, this is achieved by relaxing the complementarity condition in the contact solver. Second, we explicitly characterize the error introduced by smoothing, deriving tight analytical bounds for it. Finally, we jointly optimize a nominal trajectory and an affine feedback policy: the smoothed dynamics provide informative gradients for trajectory optimization, while the feedback policy yields tube-valued predictions over which constraints are enforced. Together, this recipe enables guaranteed constraint satisfaction and improved goal-reaching performance.

More broadly, our work points to a conceptual shift: physical correctness and gradient informativeness are fundamentally in tension. Rather than insisting that the nominal model be a best-fit approximation of the true dynamics, we deliberately allow it to be biased when this yields more informative gradients, provided that the induced deviation from the true system is explicitly characterized and compensated for. Our results further highlight the importance of exploiting the structure of model mismatch, rather than relying on loose, unstructured ℓ_2 -norm uncertainty bounds.

REFERENCES

- [1] Akshay Agrawal, Brandon Amos, Shane Barratt, Stephen Boyd, Steven Diamond, and J Zico Kolter. Differentiable convex optimization layers. *Advances in Neural Information Processing Systems*, 32, 2019.
- [2] Akshay Agrawal, Shane Barratt, Stephen Boyd, Enzo Busseti, and Walaa M Moursi. Differentiating through a cone program. *arXiv preprint arXiv:1904.09043*, 2019.
- [3] Brandon Amos and J. Zico Kolter. OptNet: Differentiable optimization as a layer in neural networks. In *Proceedings of the 34th International Conference on Machine Learning*, pages 136–145, 2017.
- [4] James Anderson, John C. Doyle, Steven H. Low, and Nikolai Matni. System level synthesis. *Annual Reviews in Control*, 47:364–393, 2019.
- [5] Mihai Anitescu. Optimization-based simulation of non-smooth rigid multibody dynamics. *Mathematical Programming*, 105(1):113–143, 2006.
- [6] Alp Aydinoglu and Michael Posa. Real-time multi-contact model predictive control via ADMM. In *2022 International Conference on Robotics and Automation (ICRA)*, pages 3414–3421, 2022.
- [7] Alp Aydinoglu, Adam Wei, Wei-Cheng Huang, and Michael Posa. Consensus complementarity control for multicontact MPC. *IEEE Transactions on Robotics*, 40: 3879–3896, 2024.
- [8] John T. Betts. Survey of numerical methods for trajectory optimization. *Journal of Guidance, Control, and Dynamics*, 21(2):193–207, 1998.
- [9] Stephen Boyd and Lieven Vandenberghe. *Convex Optimization*. Cambridge University Press, 2004. ISBN 9780521833783.
- [10] Alejandro M. Castro, Frank N. Permenter, and Xuchen Han. An unconstrained convex formulation of compliant contact. *IEEE Transactions on Robotics*, 39(2):1301–1320, 2023.
- [11] Glen Chou, Necmiye Ozay, and Dmitry Berenson. Safe output feedback motion planning from images via learned perception modules and contraction theory. In *International Workshop on the Algorithmic Foundations of Robotics*, pages 349–367, 2023.
- [12] C. Daniel Freeman, Erik Frey, Anton Raichuk, Sertan Girgin, Igor Mordatch, and Olivier Bachem. Brax–A differentiable physics engine for large scale rigid body simulation. In *35th Conference on Neural Information Processing Systems*, 2021.
- [13] Ignat Georgiev, Krishnan Srinivasan, Jie Xu, Eric Heiden, and Animesh Garg. Adaptive horizon actor-critic for policy learning in contact-rich differentiable simulation. In *Proceedings of the 41st International Conference on Machine Learning*, 2024.
- [14] Paul J. Goulart and Yuwen Chen. Clarabel: An interior-point solver for conic programs with quadratic objectives. *arXiv preprint arXiv:2405.12762*, 2024.
- [15] Bernhard Paus Graesdal, Shao Yuan Chew Chia, Tobia Marcucci, Savva Morozov, Alexandre Amice, Pablo A Parrilo, and Russ Tedrake. Towards tight convex relaxations for contact-rich manipulation. In *Proceedings of Robotics: Science and Systems (RSS)*, 2024.
- [16] Nikolaus Hansen. The CMA evolution strategy: A tutorial. *arXiv preprint arXiv:1604.00772*, 2016.
- [17] Francois R Hogan and Alberto Rodriguez. Reactive planar non-prehensile manipulation with hybrid model predictive control. *The International Journal of Robotics Research*, 39(7):755–773, 2020.
- [18] Taylor Howell, Nimrod Gileadi, Saran Tunyasuvunakool, Kevin Zakka, Tom Erez, and Yuval Tassa. Predictive sampling: Real-time behaviour synthesis with MuJoCo. *arXiv preprint arXiv:2212.00541*, 2022.
- [19] Taylor A. Howell, Simon Le Cleac'h, Jan Brüdigam, J. Zico Kolter, Mac Schwager, and Zachary Manchester. Dojo: A differentiable physics engine for robotics. *arXiv preprint arXiv:2203.00806*, 2022.
- [20] Taylor A. Howell, Simon Le Cleac'h, Sumeet Singh, Pete Florence, Zachary Manchester, and Vikas Sindhwani. Trajectory optimization with optimization-based dynamics. *IEEE Robotics and Automation Letters*, 7(3):6750–6757, 2022.
- [21] Julius Jankowski, Lara Brudermüller, Nick Hawes, and Sylvain Calinon. VP-STO: Via-point-based stochastic trajectory optimization for reactive robot behavior. *arXiv preprint arXiv:2210.04067*, 2022.
- [22] Gijeong Kim, Dongyun Kang, Joon-Ha Kim, Seungwoo Hong, and Hae-Won Park. Contact-implicit model predictive control: Controlling diverse quadruped motions without pre-planned contact modes or trajectories. *The International Journal of Robotics Research*, 44(3): 486–510, 2025.
- [23] Craig Knuth, Glen Chou, Necmiye Ozay, and Dmitry Berenson. Planning with learned dynamics: Probabilistic guarantees on safety and reachability via Lipschitz constants. *IEEE Robotics and Automation Letters*, 6(3): 5129–5136, 2021.
- [24] Craig Knuth, Glen Chou, Jamie Reese, and Joseph Moore. Statistical safety and robustness guarantees for feedback motion planning of unknown underactuated stochastic systems. In *2023 IEEE International Conference on Robotics and Automation (ICRA)*, pages 12700–12706, 2023.
- [25] Vince Kurtz, Alejandro Castro, Aykut Özgün Önol, and Hai Lin. Inverse dynamics trajectory optimization for contact-implicit model predictive control. *The International Journal of Robotics Research*, 45(1):23–40, 2026.
- [26] Simon Le Cleac'h, Mac Schwager, Zachary Manchester, Vikas Sindhwani, Pete Florence, and Sumeet Singh. Single-level differentiable contact simulation. *IEEE Robotics and Automation Letters*, 8(7):4012–4019, 2023.
- [27] Simon Le Cleac'h, Taylor A. Howell, Shuo Yang, Chi-Yen Lee, John Zhang, Arun Bishop, Mac Schwager, and Zachary Manchester. Fast contact-implicit model predictive control. *IEEE Transactions on Robotics*, 40:

- [28] Antoine P. Leeman, Johannes Köhler, Florian Messerer, Amon Lahr, Moritz Diehl, and Melanie N. Zeilinger. Fast system level synthesis: Robust model predictive control using Riccati recursions. *IFAC-PapersOnLine*, 58(18):173–180, 2024.
- [29] Antoine P. Leeman, Johannes Köhler, Andrea Zanelli, Samir Bennani, and Melanie N. Zeilinger. Robust nonlinear optimal control via system level synthesis. *IEEE Transactions on Automatic Control*, 70(7):4780–4787, 2025.
- [30] Albert H. Li, Preston Culbertson, Vince Kurtz, and Aaron D. Ames. DROP: Dexterous reorientation via online planning. In *2025 IEEE International Conference on Robotics and Automation (ICRA)*, pages 14299–14306, 2025.
- [31] D. Limon, J.M. Bravo, T. Alamo, and E.F. Camacho. Robust MPC of constrained nonlinear systems based on interval arithmetic. *IEE Proceedings - Control Theory and Applications*, 152:325–332, 2005.
- [32] Danylo Malyuta, Taylor P. Reynolds, Michael Szmuk, Thomas Lew, Riccardo Bonalli, Marco Pavone, and Behçet Açıkmeşe. Convex optimization for trajectory generation: A tutorial on generating dynamically feasible trajectories reliably and efficiently. *IEEE Control Systems Magazine*, 42(5):40–113, 2022.
- [33] Zachary Manchester, Neel Doshi, Robert J. Wood, and Scott Kuindersma. Contact-implicit trajectory optimization using variational integrators. *The International Journal of Robotics Research*, 38(12-13):1463–1476, 2019.
- [34] Tobia Marcucci, Jack Umenberger, Pablo Parrilo, and Russ Tedrake. Shortest paths in graphs of convex sets. *SIAM Journal on Optimization*, 34(1):507–532, 2024.
- [35] Matthew T. Mason. *Mechanics of Robotic Manipulation*. The MIT Press, 2001.
- [36] Louis Montaut, Quentin Le Lidec, Antoine Bambade, Vladimir Petrik, Josef Sivic, and Justin Carpentier. Differentiable collision detection: A randomized smoothing approach. In *2023 IEEE International Conference on Robotics and Automation (ICRA)*, pages 3240–3246, 2023.
- [37] Miguel Angel Zamora Mora, Momchil Peychev, Sehoon Ha, Martin Vechev, and Stelian Coros. PODS: Policy optimization via differentiable simulation. In *Proceedings of the 38th International Conference on Machine Learning*, pages 7805–7817, 2021.
- [38] João Moura, Theodoros Stouraitis, and Sethu Vijayakumar. Non-prehensile planar manipulation via trajectory optimization with complementarity constraints. In *2022 International Conference on Robotics and Automation (ICRA)*, pages 970–976, 2022.
- [39] J. Krishna Murthy, Miles Macklin, Florian Golemo, Vikram Voleti, Linda Petrini, Martin Weiss, Breandan Considine, Jérôme Parent-Lévesque, Kevin Xie, Kenny Erleben, Liam Paull, Florian Shkurti, Derek Nowrouzezahrai, and Sanja Fidler. gradSim: Differentiable simulation for system identification and visuomotor control. In *International Conference on Learning Representations*, 2021.
- [40] Rhys Newbury, Jack Collins, Kerry He, Jiahe Pan, Ingmar Posner, David Howard, and Akansel Cosgun. A review of differentiable simulators. *IEEE Access*, 12:97581–97604, 2024.
- [41] Tao Pang and Russ Tedrake. A convex quasistatic time-stepping scheme for rigid multibody systems with contact and friction. In *2021 IEEE International Conference on Robotics and Automation (ICRA)*, pages 6614–6620, 2021.
- [42] Tao Pang, H.J. Terry Suh, Lujie Yang, and Russ Tedrake. Global planning for contact-rich manipulation via local smoothing of quasi-dynamic contact models. *IEEE Transactions on Robotics*, 39(6):4691–4711, 2023.
- [43] Xue Bin Peng, Marcin Andrychowicz, Wojciech Zaremba, and Pieter Abbeel. Sim-to-real transfer of robotic control with dynamics randomization. In *2018 IEEE International Conference on Robotics and Automation (ICRA)*, pages 3803–3810, 2018.
- [44] Corrado Pezzato, Chadi Salmi, Elia Trevisan, Max Spahn, Javier Alonso-Mora, and Carlos Hernández Corbato. Sampling-based model predictive control leveraging parallelizable physics simulations. *IEEE Robotics and Automation Letters*, 10(3):2750–2757, 2025.
- [45] Yi-Ling Qiao, Junbang Liang, Vladlen Koltun, and Ming C Lin. Efficient differentiable simulation of articulated bodies. In *Proceedings of the 38th International Conference on Machine Learning*, pages 8661–8671, 2021.
- [46] Aravind Rajeswaran, Sarvjeet Ghotra, Balaraman Ravindran, and Sergey Levine. EPOpt: Learning robust neural network policies using model ensembles. In *International Conference on Learning Representations*, 2017.
- [47] John Schulman, Yan Duan, Jonathan Ho, Alex Lee, Ibrahim Awwal, Henry Bradlow, Jia Pan, Sachin Patil, Ken Goldberg, and Pieter Abbeel. Motion planning with sequential convex optimization and convex collision checking. *The International Journal of Robotics Research*, 33(9):1251–1270, 2014.
- [48] John Schulman, Filip Wolski, Prafulla Dhariwal, Alec Radford, and Oleg Klimov. Proximal policy optimization algorithms. *arXiv preprint arXiv:1707.06347*, 2017.
- [49] Yuki Shirai, Tong Zhao, H.J. Terry Suh, Huaijiang Zhu, Xinpei Ni, Jiuguang Wang, Max Simchowitz, and Tao Pang. Is linear feedback on smoothed dynamics sufficient for stabilizing contact-rich plans? In *2025 IEEE International Conference on Robotics and Automation (ICRA)*, page 11926–11932, 2025.
- [50] D. C. Sorensen. Newton’s method with a model trust region modification. *SIAM Journal on Numerical Analysis*, 19(2):409–426, 1982.
- [51] H. J. Terry Suh, Tao Pang, Tong Zhao, and Russ Tedrake. Dexterous contact-rich manipulation via the contact trust region. *The International Journal of Robotics Research*,

2026.

- [52] H.J. Terry Suh, Tao Pang, and Russ Tedrake. Bundled gradients through contact via randomized smoothing. *IEEE Robotics and Automation Letters*, 7(2):4000–4007, 2022. doi: 10.1109/LRA.2022.3146931.
- [53] H.J. Terry Suh, Max Simchowitz, Kaiqing Zhang, and Russ Tedrake. Do differentiable simulators give better policy gradients? In *Proceedings of the 39th International Conference on Machine Learning*, pages 20668–20696, 2022.
- [54] Richard S. Sutton, David McAllester, Satinder Singh, and Yishay Mansour. Policy gradient methods for reinforcement learning with function approximation. In *Advances in Neural Information Processing Systems*, volume 12, 1999.
- [55] Lieven Vandenberghe. *The CVXOPT linear and quadratic cone program solvers*, 2010.
- [56] Keenon Werling, Dalton Omens, Jeongseok Lee, Ioannis Exarchos, and C. Karen Liu. Fast and feature-complete differentiable physics for articulated rigid bodies with contact. In *Proceedings of Robotics: Science and Systems (RSS)*, 2021.
- [57] Jie Xu, Viktor Makoviychuk, Yashraj Narang, Fabio Ramos, Wojciech Matusik, Animesh Garg, and Miles Macklin. Accelerated policy learning with parallel differentiable simulation. In *International Conference on Learning Representations*, 2022.
- [58] Shenao Zhang, Wanxin Jin, and Zhaoran Wang. Adaptive barrier smoothing for first-order policy gradient with contact dynamics. In *Proceedings of the 40th International Conference on Machine Learning*, pages 41219–41243, 2023.

APPENDIX A IMPLICIT DIFFERENTIATION OF CONIC PROGRAMS

The gradient of the solution of problem (1) or (3) with respect to problem data θ can be obtained by differentiating the KKT conditions (2) with respect to θ . This leads to the linear system

$$\underbrace{\begin{bmatrix} P & A^\top & 0 \\ A & 0 & I \\ 0 & L(s) & L(z) \end{bmatrix}}_K \begin{bmatrix} \frac{\partial x}{\partial \theta} \\ \frac{\partial z}{\partial \theta} \\ \frac{\partial s}{\partial \theta} \end{bmatrix} + \begin{bmatrix} \frac{\partial P}{\partial \theta} x + \frac{\partial q}{\partial \theta} + \frac{\partial A^\top}{\partial \theta} z \\ \frac{\partial A}{\partial \theta} x - \frac{\partial b}{\partial \theta} \\ 0 \end{bmatrix} = 0,$$

where $L(s)$ is the linear operator satisfying $L(s)z = s \circ z$.

Similarly, by differentiating the KKT conditions (2) with respect to κ , the gradient of the conic program solution with respect to the complementarity value κ satisfies

$$\underbrace{\begin{bmatrix} P & A^\top & 0 \\ A & 0 & I \\ 0 & L(s) & L(z) \end{bmatrix}}_K \begin{bmatrix} \frac{\partial x}{\partial \kappa} \\ \frac{\partial z}{\partial \kappa} \\ \frac{\partial s}{\partial \kappa} \end{bmatrix} = \begin{bmatrix} 0 \\ 0 \\ e \end{bmatrix}.$$

Additionally, double derivatives can be obtained by solving

$$K \begin{bmatrix} \frac{\partial^2 x}{\partial \theta \partial \kappa} \\ \frac{\partial^2 z}{\partial \theta \partial \kappa} \\ \frac{\partial^2 s}{\partial \theta \partial \kappa} \end{bmatrix} = -\frac{\partial K}{\partial \theta} \begin{bmatrix} \frac{\partial x}{\partial \kappa} \\ \frac{\partial z}{\partial \kappa} \\ \frac{\partial s}{\partial \kappa} \end{bmatrix}.$$

APPENDIX B QUASIDYNAMIC MODEL OF CONTACT DYNAMICS

In the quasidynamic model of contact dynamics, the state is defined as

$$x = [x_a^\top \ x_o^\top]^\top,$$

where $x_a \in \mathbb{R}^{n_a}$ represents the actuated degrees of freedom (DoFs) and $x_o \in \mathbb{R}^{n_o}$ represents the unactuated object DoFs. The current timestep state x and next timestep state x^+ must satisfy:

$$K_a(x_a - u) = \tau_a(x) + \sum_{i=1}^{n_c} J_{a_i}(x)^\top \lambda_i, \quad (15a)$$

$$M_o(x) \frac{x_o^+ - x_o}{\delta t^2} = \tau_o(x) + \sum_{i=1}^{n_c} J_{o_i}(x)^\top \lambda_i, \quad (15b)$$

$$\lambda_i \in \mathcal{F}_i, \quad (15c)$$

$$\nu_{i,n} := J_{i,n}(x) (x^+ - x) + \phi_i(x) \geq 0, \quad (15d)$$

$$\nu_{i,n} \lambda_{i,n} = 0. \quad (15e)$$

Equations (15a) and (15b) describes the force balance. Here, $u \in \mathbb{R}^{n_a}$ is the control input applied to the actuated DoFs via a stiffness controller parameterized by $K_a \in \mathbb{S}_{++}^{n_a}$, and $M_o \in \mathbb{S}_{++}^{n_o}$ is the mass matrix for the unactuated object DoFs. The generalized forces $\tau_a \in \mathbb{R}^{n_a}$ and $\tau_o \in \mathbb{R}^{n_o}$ include effects such as gravity. The contact forces $\lambda_i = [\lambda_{i,n} \ \lambda_{i,t}^\top]^\top \in \mathbb{R}^d$ enter the force balance equations through the contact Jacobian

$$J_i(x) = [J_{a_i}(x) \ J_{o_i}(x)] \in \mathbb{R}^{d \times (n_a + n_o)},$$

where d is the dimension of the contact force ($d = 1$ for purely 1D contact, $d = 2$ for planar contact, and $d = 3$ for general spatial contact). The total number of contact pairs is denoted by n_c . Constraint (15c) enforces that the contact force lies within the friction cone:

$$\mathcal{F}_i = \left\{ [\lambda_{i,n} \ \lambda_{i,t}^\top]^\top \mid \|\lambda_{i,t}\|_2 \leq \mu_i \lambda_{i,n} \right\},$$

where μ_i is the coefficient of friction for the i th contact. In (15d), $\phi_i(x)$ denotes the signed distance of the i th contact at the current timestep, $\nu_{i,n}$ is its linear approximation at the next timestep. This constraint enforces non-penetration. Finally, (15e) encodes complementarity, i.e., contact force can only be applied when the signed distance is zero.

We can rewrite (15) compactly as

$$\begin{aligned} P(x) x^+ + q(x, u) - \sum_{i=1}^{n_c} J_i(x)^\top \lambda_i &= 0, \\ \nu_{i,n} &= J_{i,n}(x) (x^+ - x) + \phi_i(x), \\ \lambda_i &\in \mathcal{F}_i, \quad \nu_{i,n} \geq 0, \quad \nu_{i,n} \lambda_{i,n} = 0, \end{aligned} \quad (16)$$

where

$$\begin{aligned} P(x) &= \begin{bmatrix} K_a & 0 \\ 0 & M_o(x)/\delta t^2 \end{bmatrix}, \\ q(x, u) &= \begin{bmatrix} -K_a u - \tau_a(x) \\ -M_o(x) x_o/\delta t^2 - \tau_o(x) \end{bmatrix}. \end{aligned}$$

For general 3D systems involving rotation, the governing equations are more complicated but can still be expressed in the compact form of (16).

Conveniently, the KKT conditions of

$$\begin{aligned} \underset{x^+, \nu}{\text{minimize}} \quad & \frac{1}{2} (x^+)^T P(x) x^+ + q(x, u)^T x^+ \\ \text{subject to} \quad & \nu_i = J_i(x) (x^+ - x) + [\phi_i(x) \ 0 \ 0]^\top, \\ & \nu_i \in \mathcal{F}_i^*, \quad \forall i = 1, \dots, n_c, \end{aligned} \quad (17)$$

are

$$P(x) x^+ + q(x, u) - \sum_{i=1}^{n_c} J_i(x)^\top \lambda_i = 0, \quad (18a)$$

$$\nu_i = J_i(x) (x^+ - x) + [\phi_i(x) \ 0 \ 0]^\top, \quad (18b)$$

$$\lambda_i \in \mathcal{F}_i, \quad \nu_i \in \mathcal{F}_i^*, \quad \lambda_i \circ \nu_i = 0, \quad \forall i = 1, \dots, n_c. \quad (18c)$$

which satisfy (16). Here, \mathcal{F}_i^* denotes the dual cone of \mathcal{F}_i , defined as

$$\mathcal{F}_i^* = \left\{ [\nu_{i,n} \ \nu_{i,t}^\top]^\top \mid \|\nu_{i,t}\|_2 \leq \frac{1}{\mu_i} \nu_{i,n} \right\}.$$

Thus, solving the convex conic program (17) yields the primal and dual solutions corresponding to the next timestep state x^+ and contact forces λ_i , respectively.

The smoothed dynamics is defined implicitly by

$$\begin{aligned} \underset{x_\kappa^+, \nu}{\text{minimize}} \quad & \frac{1}{2} (x_\kappa^+)^T P(x) x_\kappa^+ + q(x, u)^T x_\kappa^+ + \kappa \sum_{i=1}^I \psi_i(\nu_{\kappa,i}) \\ \text{subject to} \quad & \nu_{\kappa,i} = J_i(x) (x_\kappa^+ - x) + [\phi_i(x) \ 0 \ 0]^\top, \\ & \forall i = 1, \dots, n_c, \end{aligned} \quad (19)$$

which has KKT conditions

$$P(x) x_\kappa^+ + q(x, u) - \sum_{i=1}^{n_c} J_i(x)^\top \lambda_{\kappa,i} = 0, \quad (20a)$$

$$\nu_{\kappa,i} = J_i(x) (x_\kappa^+ - x) + [\phi_i(x) \ 0 \ 0]^\top, \quad (20b)$$

$$\begin{aligned} \lambda_{\kappa,i} &\in \mathcal{F}_i, & \nu_{\kappa,i} &\in \mathcal{F}_i^*, & \lambda_{\kappa,i} \circ \nu_{\kappa,i} &= \kappa e, \\ &\forall i = 1, \dots, n_c. & & & & \end{aligned} \quad (20c)$$

It is worth noting that this quasidynamic model, due to its neglect of velocity effects, cannot accurately capture the principle of maximum dissipation [10], which governs the tangential frictional force under sliding contact.

APPENDIX C PROOF OF THEOREM 1

Notice that the deviation between the true dynamics $f_0(x, u)$ and the smoothed dynamics $f_\kappa(x, u)$ is given by

$$f_0(x, u) = f_\kappa(x, u) + \int_\kappa^0 \frac{\partial f_\kappa(x, u)}{\partial \kappa} d\kappa. \quad (21)$$

To compute $\partial f_\kappa(x, u)/\partial \kappa$, which is equivalent to $\partial x_\kappa/\partial \kappa$, we differentiate (20a) with respect to κ , yielding

$$P(x) \frac{\partial x_\kappa^+}{\partial \kappa} - \sum_{i=1}^{n_c} J_i(x)^\top \frac{\partial \lambda_{\kappa,i}}{\partial \kappa} = 0.$$

Substituting into (21) yields

$$f_0(x, u) = f_\kappa(x, u) - P(x)^{-1} \sum_{i=1}^{n_c} J_i(x)^\top \int_0^\kappa \frac{\partial \lambda_{\kappa,i}}{\partial \kappa} d\kappa.$$

Hence, we need to show that

$$\left(\int_0^\kappa \frac{\partial \lambda_{\kappa,i}}{\partial \kappa} d\kappa \right) \in \left(\frac{\partial \lambda_{\kappa,i}}{\partial \kappa} \kappa w_i \right), \quad (22)$$

where $w_i \in [1, 2]$.

From

$$\lambda_{\kappa,i} = \frac{\kappa}{\nu_{\kappa,i,n}^2/\mu_i^2 - \|\nu_{\kappa,i,t}\|_2^2} \begin{bmatrix} \nu_{\kappa,i,n}/\mu_i^2 \\ -\nu_{\kappa,i,t} \end{bmatrix},$$

we have

$$\frac{\partial \lambda_{\kappa,i}}{\partial \kappa} = (\text{diag}(\nu_{\kappa,i}) + c_{\kappa,i} J_i P^{-1} J_i^\top)^\dagger \frac{1}{\kappa} \text{diag}(\nu_{\kappa,i}) \lambda_{\kappa,i},$$

where

$$c_{\kappa,i} = \frac{2}{\kappa} \text{diag}(\nu_{\kappa,i}) \lambda_{\kappa,i} \lambda_{\kappa,i}^\top - \text{diag}(\lambda_{\kappa,i}).$$

In the normal direction, we simply have

$$\frac{\partial \lambda_{\kappa,i,n}}{\partial \kappa} = (\nu_{\kappa,i,n} + \lambda_{\kappa,i,n} J_{i,n} P^{-1} J_{i,n}^\top)^{-1}.$$

We will show separately that (22) satisfies in the normal and tangential direction. But before that, we need the following lemma.

Lemma 1. With the assumption that $J_i P^{-1} J_j^\top = 0$ for all $i \neq j$, the vector quantity

$$\nu_{\kappa,i} - J_i P^{-1} J_i^\top \lambda_{\kappa,i}$$

is independent of κ .

Proof: Left-multiplying (20a) by $J_j P^{-1}$ yields

$$J_j x_\kappa^+ + J_j P^{-1} q(x, u) - \sum_{i=1}^{n_c} J_j P^{-1} J_i^\top \lambda_{\kappa,i} = 0.$$

Due to the assumption that $J_i P^{-1} J_j^\top = 0$ for all $i \neq j$, we have

$$J_i x_\kappa^+ + J_i P^{-1} q(x, u) - J_i P^{-1} J_i^\top \lambda_{\kappa,i} = 0.$$

Substituting in $J_i x_\kappa^+ = \nu_{\kappa,i} + J_i x - [\phi_i(x) \ 0 \ 0]^\top$ from (20b), we obtain

$$\nu_{\kappa,i}^+ - J_i P^{-1} J_i^\top \lambda_{\kappa,i} = -J_i P^{-1} q(x, u) - J_i x + [\phi_i(x) \ 0 \ 0]^\top.$$

The right-hand side of the equation is independent of κ . Hence, the left-hand side is also independent of κ . \blacksquare

Corollary 1. With the assumption that $J_i P^{-1} J_j^\top = 0$ for all $i \neq j$, the scalar quantity

$$\nu_{\kappa,i,n} - \lambda_{\kappa,i,n} J_{i,n} P^{-1} J_{i,n}^\top$$

is independent of κ .

A. Bounds for Normal Component

We show that the normal component of (22) is true. In the normal direction, the left-hand side of (22) is

$$\int_0^\kappa (\nu_{\kappa,i,n} + \lambda_{\kappa,i,n} J_{i,n} P^{-1} J_{i,n}^\top)^{-1} d\kappa. \quad (23)$$

From the arithmetic mean-geometric mean (AM-GM) inequality, we have

$$\begin{aligned} \frac{1}{2} (\nu_{\kappa,i,n} + \lambda_{\kappa,i,n} J_{i,n} P^{-1} J_{i,n}^\top) &\geq (\nu_{\kappa,i,n} \lambda_{\kappa,i,n} J_{i,n} P^{-1} J_{i,n}^\top)^{\frac{1}{2}} \\ &= (\kappa J_{i,n} P^{-1} J_{i,n}^\top)^{\frac{1}{2}}, \end{aligned}$$

with equality satisfied when

$$\nu_{\kappa,i,n} = \lambda_{\kappa,i,n} J_{i,n} P^{-1} J_{i,n}^\top.$$

Hence, we have bounds on the integrand of (23):

$$0 \leq (\nu_{\kappa,i,n} + \lambda_{\kappa,i,n} J_{i,n} P^{-1} J_{i,n}^\top)^{-1} \leq \frac{1}{2} (\kappa J_{i,n} P^{-1} J_{i,n}^\top)^{-\frac{1}{2}}. \quad (24)$$

The upper bound of (24) is achieved when an (x, u) pair results in

$$\nu_{\kappa,i,n} = \lambda_{\kappa,i,n} J_{i,n} P^{-1} J_{i,n}^\top = (\kappa J_{i,n} P^{-1} J_{i,n}^\top)^{\frac{1}{2}}. \quad (25)$$

From the fact that

$$\nu_{\kappa,i,n} - \lambda_{\kappa,i,n} J_{i,n} P^{-1} J_{i,n}^\top = 0$$

and utilizing Corollary 1, (25) must satisfy for all κ values under the same (x, u) pair. Hence, (23) is bounded above tightly as follows:

$$\begin{aligned} &\int_0^\kappa (\nu_{\kappa,i,n} + \lambda_{\kappa,i,n} J_{i,n} P^{-1} J_{i,n}^\top)^{-1} d\kappa \\ &\leq \int_0^\kappa \frac{1}{2} (\kappa J_{i,n} P^{-1} J_{i,n}^\top)^{-\frac{1}{2}} d\kappa \\ &= \frac{1}{2} (J_{i,n} P^{-1} J_{i,n}^\top)^{-\frac{1}{2}} 2\kappa^{\frac{1}{2}} \\ &= (\nu_{\kappa,i,n} + \lambda_{\kappa,i,n} J_{i,n} P^{-1} J_{i,n}^\top)^{-1} 2\kappa. \end{aligned}$$

This establishes the upper bound of the normal component of (22) with $w_i = 2$.

The lower bound of (24) is achieved when an (x, u) pair results in

$$\nu_{\kappa,i,n} + \lambda_{\kappa,i,n} J_{i,n} P^{-1} J_{i,n}^\top = C, \quad (26)$$

in the limit of $C \rightarrow \infty$. From the fact that

$$\nu_{\kappa,i,n} - \lambda_{\kappa,i,n} J_{i,n} P^{-1} J_{i,n}^\top = \pm C$$

and utilizing Corollary 1, (26) must satisfy for all κ values under the same (x, u) pair. Hence, (23) is bounded below tightly as follows:

$$\begin{aligned} & \int_0^\kappa (\nu_{\kappa,i,n} + \lambda_{\kappa,i,n} J_{i,n} P^{-1} J_{i,n}^\top)^{-1} d\kappa \\ & \geq \int_0^\kappa C^{-1} d\kappa = C^{-1} \kappa \\ & = (\nu_{\kappa,i,n} + \lambda_{\kappa,i,n} J_{i,n} P^{-1} J_{i,n}^\top)^{-1} \kappa. \end{aligned}$$

This establishes the lower bound of the normal component of (22) with $w_i = 1$.

B. Bounds for Tangential Component

We show that the tangential component of (22) is true. The left-hand side of (22) is

$$\int_0^\kappa (\text{diag}(\nu_{\kappa,i}) + c_{\kappa,i} J_i P^{-1} J_i^\top)^\dagger \frac{1}{\kappa} \text{diag}(\nu_{\kappa,i}) \lambda_{\kappa,i} d\kappa. \quad (27)$$

The upper bound of the tangential component of (27) is achieved when an (x, u) pair results in

$$\|\nu_{\kappa,i,t}\|_2 = \nu_{\kappa,i,n} / \mu_i, \quad \nu_{\kappa,i,n} = \sqrt{\frac{\kappa \mu_i^2}{\mu_i^2 + 1}}. \quad (28)$$

From the fact that

$$\nu_{\kappa,i} - J_i P^{-1} J_i^\top \lambda_{\kappa,i} = \infty$$

and utilizing Lemma 1, (28) must satisfy for all κ values under the same (x, u) pair. It follows that

$$\begin{aligned} & (\text{diag}(\nu_{\kappa,i}) + c_{\kappa,i} J_i P^{-1} J_i^\top)^\dagger \frac{1}{\kappa} \text{diag}(\nu_{\kappa,i}) \lambda_{\kappa,i} \\ & = \begin{bmatrix} \frac{1}{2} \mu_i (\mu_i^2 + 1)^{-\frac{1}{2}} \kappa^{-\frac{1}{2}} \\ \xi_{\kappa,i,t} \end{bmatrix}, \end{aligned}$$

with $\|\xi_{\kappa,i,t}\|_2 = \frac{1}{2} (\mu_i^2 + 1)^{-\frac{1}{2}} \kappa^{-\frac{1}{2}}$. Hence, the tangential component of bounded above tightly by

$$\begin{aligned} & \int_0^\kappa \frac{1}{2} (\mu_i^2 + 1)^{-\frac{1}{2}} \kappa^{-\frac{1}{2}} d\kappa = \frac{1}{2} (\mu_i^2 + 1)^{-\frac{1}{2}} 2 \kappa^{\frac{1}{2}} \\ & = \frac{1}{2} (\mu_i^2 + 1)^{-\frac{1}{2}} \kappa^{-\frac{1}{2}} 2\kappa. \end{aligned}$$

This establishes the upper bound of the tangential component of (22) with $w_i = 2$.

The lower bound of the tangential component of (27) is achieved when an (x, u) pair results in

$$\nu_{\kappa,i,t} = 0, \quad \lambda_{\kappa,i,t} = 0. \quad (29)$$

From the fact that

$$\nu_{\kappa,i} - J_i P^{-1} J_i^\top \lambda_{\kappa,i} = 0$$

and utilizing Lemma 1, (29) must satisfy for all κ values under the same (x, u) pair. It follows that

$$(\text{diag}(\nu_{\kappa,i}) + c_{\kappa,i} J_i P^{-1} J_i^\top)^\dagger \frac{1}{\kappa} \text{diag}(\nu_{\kappa,i}) \lambda_{\kappa,i} = \begin{bmatrix} \xi_{\kappa,i,n} \\ 0 \end{bmatrix}.$$

Hence, the tangential component of bounded below tightly by 0. This establishes the lower bound of the tangential component of (22) with $w_i = 1$.

APPENDIX D

PROOF OF THEOREM 2

The proof here is similar to [4, Thm 2.1]. For the LTV approximation of the true dynamics (7) rewritten here as

$$x_{k+1} = f_\kappa(x_k, u_k) + E_\kappa(x_k, u_k) w,$$

about the nominal trajectory $\mathbf{z} = [z_0^\top \cdots z_N^\top]^\top$ and $\mathbf{v} = [v_0^\top \cdots v_{N-1}^\top]^\top$, we have

$$x_{k+1} - z_k = A_k (x_k - z_k) + B_k (u_k - v_k) + E_k w,$$

where $A_k = \partial f_\kappa(z_k, v_k) / \partial z$, $B_k = \partial f_\kappa(z_k, v_k) / \partial v$, and $E_k = E_\kappa(z_k, v_k)$. This can be written in block matrix form as

$$\mathbf{x} - \mathbf{z} = \mathbf{Z} \mathbf{A} (\mathbf{x} - \mathbf{z}) + \mathbf{Z} \mathbf{B} (\mathbf{u} - \mathbf{v}) + \mathbf{Z} \mathbf{E} \mathbf{w},$$

where \mathbf{Z} is the block-downshift operator, i.e., a matrix with identity matrices along its first block sub-diagonal and zeros elsewhere, and $\mathbf{A} = \text{blkdiag}(A_1, \dots, A_{N-1}, 0)$, $\mathbf{B} = \text{blkdiag}(B_1, \dots, B_{N-1}, 0)$. Furthermore, with causal feedback policies of the form

$$\mathbf{u} - \mathbf{v} = \mathbf{K}(\mathbf{x} - \mathbf{z}),$$

where \mathbf{K} is a block lower-triangular matrix, we have

$$\begin{bmatrix} \mathbf{x} - \mathbf{z} \\ \mathbf{u} - \mathbf{v} \end{bmatrix} := \begin{bmatrix} \Phi^x \\ \Phi^u \end{bmatrix} \mathbf{w} = \begin{bmatrix} (\mathbf{I} - \mathbf{Z}(\mathbf{A} + \mathbf{B}\mathbf{K}))^{-1} \mathbf{Z} \mathbf{E} \\ \mathbf{K}(\mathbf{I} - \mathbf{Z}(\mathbf{A} + \mathbf{B}\mathbf{K}))^{-1} \mathbf{Z} \mathbf{E} \end{bmatrix} \mathbf{w}.$$

It is then easily seen that

$$\begin{aligned} & [\mathbf{I} - \mathbf{Z} \mathbf{A} \quad -\mathbf{Z} \mathbf{B}] \begin{bmatrix} \Phi^x \\ \Phi^u \end{bmatrix} \\ & = [\mathbf{I} - \mathbf{Z} \mathbf{A} \quad -\mathbf{Z} \mathbf{B}] \begin{bmatrix} (\mathbf{I} - \mathbf{Z}(\mathbf{A} + \mathbf{B}\mathbf{K}))^{-1} \mathbf{Z} \mathbf{E} \\ \mathbf{K}(\mathbf{I} - \mathbf{Z}(\mathbf{A} + \mathbf{B}\mathbf{K}))^{-1} \mathbf{Z} \mathbf{E} \end{bmatrix} \\ & = (\mathbf{I} - \mathbf{Z} \mathbf{A} - \mathbf{Z} \mathbf{B} \mathbf{K}) (\mathbf{I} - \mathbf{Z}(\mathbf{A} + \mathbf{B}\mathbf{K}))^{-1} \mathbf{Z} \mathbf{E} \\ & = \mathbf{Z} \mathbf{E}, \end{aligned}$$

which is equivalent to

$$\begin{aligned} \Phi_{k+1,j}^x &= A_k \Phi_{k,j}^x + B_k \Phi_{k,j}^u, \quad \forall k = j+1, \dots, N-1, \\ \Phi_{j+1,j}^x &= E_j, \end{aligned}$$

for all $j = 0, \dots, N-1$.

We next show that $\mathbf{K} = \Phi^u(\Phi^x)^{-1}$ achieves the desired response. Such a \mathbf{K} results in

$$\begin{aligned} \mathbf{x} - \mathbf{z} &= (\mathbf{I} - \mathbf{Z}(\mathbf{A} + \mathbf{B}\Phi^u(\Phi^x)^{-1}))^{-1} \mathbf{Z} \mathbf{E} \mathbf{w} \\ &= (((\mathbf{I} - \mathbf{Z} \mathbf{A}) \Phi^x - \mathbf{Z} \mathbf{B} \Phi^u(\Phi^x)^{-1})^{-1} \mathbf{Z} \mathbf{E} \mathbf{w} \\ &= \Phi^x((\mathbf{I} - \mathbf{Z} \mathbf{A}) \Phi^x - \mathbf{Z} \mathbf{B} \Phi^u)^{-1} \mathbf{Z} \mathbf{E} \mathbf{w} \\ &= \Phi^x(\mathbf{Z} \mathbf{E})^{-1} \mathbf{Z} \mathbf{E} \mathbf{w} \\ &= \Phi^x \mathbf{w}. \end{aligned}$$

We also have

$$\begin{aligned}\mathbf{u} - \mathbf{v} &= \Phi^u(\Phi^x)^{-1}(\mathbf{x} - \mathbf{z}) \\ &= \Phi^u(\Phi^x)^{-1}(\Phi^x \mathbf{w}) \\ &= \Phi^u \mathbf{w}.\end{aligned}$$

APPENDIX E EFFICIENT SOLVER FOR PROBLEM (13)

We derive an efficient algorithm for solving (30). The algorithm derived here is based on [28], with some modifications to allow for state/input-dependent disturbance matrix and nonzero-centered disturbance

$$w \in \mathcal{W} \subseteq \{w \in \mathbb{R}^{n_c} \mid \|w - w_c\|_p \leq w_r\}.$$

We outer approximate the disturbance set \mathcal{W} with a ℓ_2 -norm ball centered around w_c so that $p = 2$. From $1/p + 1/q = 1$, the dual norm exponent q is equal to 2.

To write the optimization problem (30) concisely, we introduce auxiliary variables $\beta_{k,j}$ defined as

$$\beta_{k,j} = H_{k,j}(\Phi) = (\|G_k \begin{bmatrix} \Phi_{k,j}^x \\ \Phi_{k,j}^u \end{bmatrix}\|_{\text{row},2})^2 \in \mathbb{R}^{n_c}, \quad (31a)$$

$$\beta_{f,j} = H_{f,j}(\Phi) = (\|G_f \Phi_{N,j}^x\|_{\text{row},2})^2 \in \mathbb{R}^{n_f}. \quad (31b)$$

Here, the operation $(\cdot)^2$ is defined elementwise. We define

$$h_k^{\text{ct}}(\beta) = \sum_{j=0}^{k-1} w_r (\beta_{k,j} + \epsilon \mathbf{1}_{n_c})^{\frac{1}{2}} \in \mathbb{R}^{n_c}, \quad (32a)$$

$$h_f^{\text{ct}}(\beta) = \sum_{j=0}^{N-1} w_r (\beta_{f,j} + \epsilon \mathbf{1}_{n_f})^{\frac{1}{2}} \in \mathbb{R}^{n_f}. \quad (32b)$$

Here, the operation $(\cdot)^{\frac{1}{2}}$ is defined elementwise, and a fixed constant $\epsilon > 0$ is to circumvent points of non-differentiability. We also define

$$h_k^{\text{cs}}(\Phi) = \sum_{j=0}^{k-1} G_k \begin{bmatrix} \Phi_{k,j}^x \\ \Phi_{k,j}^u \end{bmatrix} w_c \in \mathbb{R}^{n_c}, \quad (33a)$$

$$h_f^{\text{cs}}(\Phi) = \sum_{j=0}^{N-1} G_f \Phi_{N,j}^x w_c \in \mathbb{R}^{n_f}. \quad (33b)$$

We define $\mathbf{y} = (\delta \mathbf{z}, \delta \mathbf{v})$ and summarize the optimization problem (30) as

$$\min_{\mathbf{y}, \Phi, \beta} J(\mathbf{y}) + \mathcal{J}(\Phi), \quad (34a)$$

$$\text{s.t. } f(\mathbf{y}) = 0, \quad (34b)$$

$$D(\Phi, \mathbf{y}) = 0, \quad (34c)$$

$$h^{\text{cs}}(\Phi) + h^{\text{ct}}(\beta) + h(\mathbf{y}) \leq 0, \quad (34d)$$

$$H(\Phi) - \beta = 0, \quad (34e)$$

$$g(\mathbf{y}) \leq 0. \quad (34f)$$

The constraint (34b) encodes the nominal dynamics (30b), and the constraint (34c) encodes the disturbance propagation (30c). Inequality (34d) captures the tightened constraints (30d)–(30e). Constraint (34e) captures the nonlinear relationship (31) between β and Φ . Constraint (34f) encodes additional constraints such as (30f).

We further define $\tilde{\mathcal{J}}$ as a composition function condensing the disturbance propagation (34c), such that $\tilde{\mathcal{J}}(\Phi^u, \mathbf{y}) = \mathcal{J}(\Phi)$ for any Φ with $D(\Phi, \mathbf{y}) = 0$. We do the same for \tilde{h}^{cs} and \tilde{H} . The results in a more compact optimization problem:

$$\begin{aligned}\min_{\mathbf{y}, \Phi^u, \beta} \quad & J(\mathbf{y}) + \tilde{\mathcal{J}}(\Phi^u, \mathbf{y}), \\ \text{s.t.} \quad & f(\mathbf{y}) = 0, \\ & \tilde{h}^{\text{cs}}(\Phi^u) + h^{\text{ct}}(\beta) + h(\mathbf{y}) \leq 0, \\ & \tilde{H}(\Phi^u) - \beta = 0, \\ & g(\mathbf{y}) \leq 0.\end{aligned} \quad (35)$$

The Lagrangian of (35) is given by

$$\begin{aligned}\mathcal{L}(\mathbf{y}, \Phi^u, \beta, \lambda, \mu, \eta) = & J(\mathbf{y}) + \tilde{\mathcal{J}}(\Phi^u, \mathbf{y}) + \lambda^\top f(\mathbf{y}) \\ & + \mu^\top (\tilde{h}^{\text{cs}}(\Phi^u) + h^{\text{ct}}(\beta) + h(\mathbf{y})) \\ & + \eta^\top (\tilde{H}(\Phi^u) - \beta) + \gamma^\top g(\mathbf{y}).\end{aligned} \quad (36)$$

with λ , μ , and η the dual variables. The KKT conditions of

$$\min_{\delta \mathbf{z}, \delta \mathbf{v}, \Phi^x, \Phi^u} J(\mathbf{z} + \delta \mathbf{z}, \mathbf{v} + \delta \mathbf{v}) + \mathcal{J}(\Phi^x, \Phi^u) \quad (30a)$$

$$\text{s.t. } \delta z_{k+1} = A_k \delta z_k + B_k \delta v_k, \quad \delta z_0 = 0, \quad (30b)$$

$$\Phi_{k+1,j}^x = A_k \Phi_{k,j}^x + B_k \Phi_{k,j}^u, \quad \Phi_{j+1,j}^x = E_j + \frac{\partial E_j}{\partial z} \delta z_j + \frac{\partial E_j}{\partial v} \delta v_j, \quad (30c)$$

$$\sum_{j=0}^{k-1} G_k \begin{bmatrix} \Phi_{k,j}^x \\ \Phi_{k,j}^u \end{bmatrix} w_c + w_r \|G_k \begin{bmatrix} \Phi_{k,j}^x \\ \Phi_{k,j}^u \end{bmatrix}\|_{\text{row},q} + G_k \begin{bmatrix} z_k + \delta z_k \\ v_k + \delta v_k \end{bmatrix} + g_k \leq 0, \quad (30d)$$

$$\sum_{j=0}^{N-1} G_f \Phi_{N,j}^x w_c + w_r \|G_f \Phi_{N,j}^x\|_{\text{row},q} + G_f (z_N + \delta z_N) + g_f \leq 0, \quad (30e)$$

$$\|\delta \mathbf{z}\| \leq \varepsilon, \quad \|\delta \mathbf{v}\| \leq \varepsilon. \quad (30f)$$

(35) are given by

$$\nabla J(\mathbf{y}) + \nabla_{\mathbf{y}} \tilde{\mathcal{J}}(\Phi^u, \mathbf{y}) + \nabla f(\mathbf{y}) \lambda + \nabla h(\mathbf{y}) \mu = 0, \quad (37a)$$

$$\nabla_{\Phi^u} \tilde{\mathcal{J}}(\Phi^u, \mathbf{y}) + \nabla \tilde{h}^{cs}(\Phi^u) \mu + \nabla \tilde{H}(\Phi^u) \eta = 0, \quad (37b)$$

$$\nabla h^{ct}(\beta) \mu - \eta = 0, \quad (37c)$$

$$f(\mathbf{y}) = 0, \quad (37d)$$

$$0 \leq \mu \perp \tilde{h}^{cs}(\Phi^u) + h^{ct}(\beta) + h(\mathbf{y}) \leq 0, \quad (37e)$$

$$\tilde{H}(\Phi^u) - \beta = 0. \quad (37f)$$

$$0 \leq \gamma \perp g(\mathbf{y}) \leq 0. \quad (37g)$$

The key idea of the algorithm is to partition the KKT conditions (37) into two subsets and solve them alternately. In particular, the subset of necessary conditions (37a), (37c), (37d), (37e), (37g) with fixed $\bar{\Phi}^u$ and $\bar{\beta}$, corresponds to a nominal trajectory optimization:

$$\nabla J(\mathbf{y}) + \nabla_{\mathbf{y}} \tilde{\mathcal{J}}(\bar{\Phi}^u, \mathbf{y}) + \nabla f(\mathbf{y}) \lambda + \nabla h(\mathbf{y}) \mu = 0, \quad (38a)$$

$$\nabla h^{ct}(\bar{\beta}) \mu - \eta = 0, \quad (38b)$$

$$f(\mathbf{y}) = 0, \quad (38c)$$

$$0 \leq \mu \perp \tilde{h}^{cs}(\bar{\Phi}^u) + h^{ct}(\bar{\beta}) + h(\mathbf{y}) \leq 0, \quad (38d)$$

$$0 \leq \gamma \perp g(\mathbf{y}) \leq 0. \quad (38e)$$

The solution to (38) yields $\bar{\mathbf{y}}$, $\bar{\mu}$, and $\bar{\eta}$, which are used to solve the remaining necessary conditions (37b) and (37f), corresponding to an uncertainty tube optimization:

$$\nabla_{\Phi^u} \tilde{\mathcal{J}}(\Phi^u, \bar{\mathbf{y}}) + \nabla \tilde{h}^{cs}(\Phi^u) \bar{\mu} + \nabla \tilde{H}(\Phi^u) \bar{\eta} = 0, \quad (39a)$$

$$\tilde{H}(\Phi) - \beta = 0. \quad (39b)$$

The solution to (39) yields a new fixed $\bar{\Phi}^u$ and $\bar{\beta}$, which are used to solve (38) again. The alternation continues until the KKT conditions (37) are all satisfied.

A. Uncertainty Tube Optimization

The solution to (39) can be obtained by solving the following optimization problem:

$$\min_{\Phi} \quad \mathcal{J}(\Phi) + \bar{\mu}^T h^{cs}(\Phi) + \bar{\eta}^T H(\Phi),$$

$$\text{s.t.} \quad D(\Phi, \bar{\mathbf{y}}) = 0,$$

or equivalently

$$\min_{\Phi} \quad \sum_{j=0}^{N-1} \left(\sum_{k=j+1}^{N-1} \text{Tr} \left(\begin{bmatrix} \Phi_{k,j}^x \\ \Phi_{k,j}^u \end{bmatrix}^\top P_{k,j} \begin{bmatrix} \Phi_{k,j}^x \\ \Phi_{k,j}^u \end{bmatrix} + 2p_{k,j}^\top \begin{bmatrix} \Phi_{k,j}^x \\ \Phi_{k,j}^u \end{bmatrix} \right) + \text{Tr} \left(\Phi_{N,j}^x P_{N,j} \Phi_{N,j}^x + 2p_{N,j}^\top \Phi_{N,j}^x \right) \right),$$

$$\text{s.t.} \quad \Phi_{k+1,j}^x = A_k \Phi_{k,j}^x + B_k \Phi_{k,j}^u, \\ \Phi_{j+1,j}^x = E_j + \frac{\partial E_j}{\partial z} \bar{z}_j + \frac{\partial E_j}{\partial v} \bar{v}_j,$$

where

$$P_{k,j} = \begin{bmatrix} \bar{Q} & 0 \\ 0 & \bar{R} \end{bmatrix} + G_k^\top \text{diag}(\bar{\eta}_{k,j}) G_k, \quad p_{k,j} = \frac{1}{2} G_k^\top \bar{\mu}_k w_c^\top,$$

$$P_{N,j} = \bar{Q}_f + G_f^\top \text{diag}(\bar{\eta}_{N,j}) G_f, \quad p_{N,j} = \frac{1}{2} G_f^\top \bar{\mu}_N w_c^\top.$$

This can be via using N independent Riccati recursions [28]. Each Riccati recursion solves for

$$\begin{aligned} \min_{\Phi} \quad & \sum_{k=j+1}^{N-1} \text{Tr} \left(\begin{bmatrix} \Phi_{k,j}^x \\ \Phi_{k,j}^u \end{bmatrix}^\top P_{k,j} \begin{bmatrix} \Phi_{k,j}^x \\ \Phi_{k,j}^u \end{bmatrix} + 2p_{k,j}^\top \begin{bmatrix} \Phi_{k,j}^x \\ \Phi_{k,j}^u \end{bmatrix} \right) \\ & + \text{Tr} \left(\Phi_{N,j}^x P_{N,j} \Phi_{N,j}^x + 2p_{N,j}^\top \Phi_{N,j}^x \right), \\ \text{s.t.} \quad & \Phi_{k+1,j}^x = A_k \Phi_{k,j}^x + B_k \Phi_{k,j}^u, \\ & \Phi_{j+1,j}^x = E_j + \frac{\partial E_j}{\partial z} \bar{z}_j + \frac{\partial E_j}{\partial v} \bar{v}_j. \end{aligned}$$

We partition $P_{k,j}$ and $p_{k,j}$ as

$$P_{k,j} = \begin{bmatrix} P_{k,j}^{xx} & P_{k,j}^{xu} \\ P_{k,j}^{ux} & P_{k,j}^{uu} \end{bmatrix}, \quad p_{k,j} = \begin{bmatrix} p_{k,j}^x \\ p_{k,j}^u \end{bmatrix}.$$

The Riccati recursion starts by initializing

$$S_{N,j} = P_{N,j}, \quad s_{N,j} = p_{N,j}.$$

Followed by a backward pass for $k = N-1, \dots, j+1$:

$$\begin{aligned} M_{k,j} &= P_{k,j}^{uu} + B_k^\top S_{k+1,j} B_k, \\ F_{k,j} &= P_{k,j}^{ux} + B_k^\top S_{k+1,j} A_k, \\ f_{k,j} &= p_{k,j}^u + B_k^\top s_{k+1,j}, \\ H_{k,j} &= P_{k,j}^{xx} + A_k^\top S_{k+1,j} A_k, \\ h_{k,j} &= p_{k,j}^x + A_k^\top s_{k+1,j}, \\ K_{k,j} &= -M_{k,j}^{-1} F_{k,j}, \quad k_{k,j} = -M_{k,j}^{-1} f_{k,j}, \\ S_{k,j} &= H_{k,j} + F_{k,j}^\top K_{k,j}, \quad s_{k,j} = h_{k,j} + F_{k,j}^\top k_{k,j}. \end{aligned}$$

Followed by a forward pass starting from $\Phi_{j+1,j}^x = E_j + \frac{\partial E_j}{\partial z} \bar{z}_j + \frac{\partial E_j}{\partial v} \bar{v}_j$ and for $k = j+1, \dots, N-1$:

$$\begin{aligned} \Phi_{k,j}^u &= K_{k,j} \Phi_{k,j}^x + k_{k,j}, \\ \Phi_{k+1,j}^x &= A_k \Phi_{k,j}^x + B_k \Phi_{k,j}^u. \end{aligned}$$

The resulting optimal value of the objective is

$$\sum_{j=0}^{N-1} \text{Tr} \left(\Phi_{j+1,j}^x S_{j+1,j} \Phi_{j+1,j}^x \right).$$

Once solved, the value of β is then obtained by evaluating (39b) and (31).

B. Nominal Trajectory Optimization

The solution to (38) can be obtained by solving a nominal trajectory optimization problem:

$$\begin{aligned} \min_{\delta \mathbf{z}, \delta \mathbf{v}} \quad & J(\mathbf{z} + \delta \mathbf{z}, \mathbf{v} + \delta \mathbf{v}) \\ & + \text{Tr} \left(\begin{bmatrix} \delta z_j \\ \delta v_j \end{bmatrix}^\top \begin{bmatrix} \frac{\partial E_j}{\partial z} & \frac{\partial E_j}{\partial v} \end{bmatrix}^\top S_{j+1,j} \begin{bmatrix} \frac{\partial E_j}{\partial z} & \frac{\partial E_j}{\partial v} \end{bmatrix} \begin{bmatrix} \delta z_j \\ \delta v_j \end{bmatrix} \right), \\ \text{s.t.} \quad & \delta z_{k+1} = A_k \delta z_k + B_k \delta v_k, \quad \delta z_0 = 0, \\ & h_k^{cs}(\bar{\Phi}) + h_k^{ct}(\bar{\beta}) + G_k \begin{bmatrix} z_k + \delta z_k \\ v_k + \delta v_k \end{bmatrix} + g_k \leq 0, \\ & h_N^{cs}(\bar{\Phi}) + h_N^{ct}(\bar{\beta}) + G_f (z_N + \delta z_N) + g_f \leq 0, \\ & \|\delta \mathbf{z}\| \leq \varepsilon, \quad \|\delta \mathbf{v}\| \leq \varepsilon. \end{aligned}$$

This problem is a QP. Once solved, the value of η is then obtained by evaluating (38b) and (32),

$$\begin{aligned}\eta_{k,j} &= \frac{1}{2} w_r (\beta_{k,j} + \epsilon \mathbf{1}_{n_c})^{-\frac{1}{2}} \odot \mu_k, \\ \eta_{f,j} &= \frac{1}{2} w_r (\beta_{f,j} + \epsilon \mathbf{1}_{n_f})^{-\frac{1}{2}} \odot \mu_N.\end{aligned}$$

Here, the operation $(\cdot)^{-\frac{1}{2}}$ is applied elementwise, and \odot denotes elementwise multiplication.

The algorithm alternates between uncertainty tube optimization, which uses Riccati recursions, and nominal trajectory optimization, which solves a QP, until convergence. Both the Riccati recursions and QP solves can benefit from GPU acceleration to reduce the algorithm solve time.

APPENDIX F DETAILED RESULTS ON TABLE II

Fig. 7 shows the goal error distribution for bimanual planar bucket manipulation over 1000 experiments. Without replanning (Fig. 7a), our method achieves lower goal error than TO-CTR because it can predict the outcome of rollouts under true hybrid dynamics. However, this reduction is modest, as the planning horizon is too short for smoothing errors to accumulate enough to invalidate the TO-CTR trajectory.

With MPC-style replanning (Fig. 7b), where both methods use a horizon of one, the goal errors are indistinguishable due to the short horizon. Nevertheless, our method without replanning, using the synthesized affine feedback controller, is computationally cheaper online and achieves lower goal error than both MPC-based methods.

Table II also indicates that several TO-CTR rollouts on the true hybrid dynamics result in constraint violations, whereas our method can certify constraint satisfaction under the true hybrid dynamics. These violations manifest as robot collisions (Fig. 8) or as the bucket falling off the supporting table (Fig. 9). In both cases, the nominal trajectories generated by TO-CTR are feasible under the smoothed model; however, executing the nominal control sequences on the true hybrid dynamics leads to constraint violations. In contrast, our method certifies constraint satisfaction for the true hybrid dynamics. Furthermore, as shown in Fig. 9b, our method optimizes a policy that minimizes the tube, thereby keeping the nominal trajectory and the true rollout closer compared to TO-CTR.

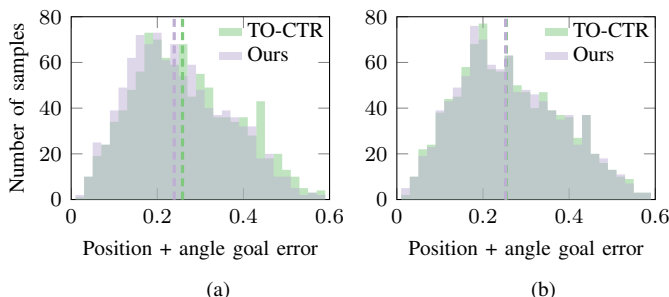


Figure 7. Goal position error plus goal angle error for bimanual planar bucket manipulation. (a) Without replanning. (b) With MPC.

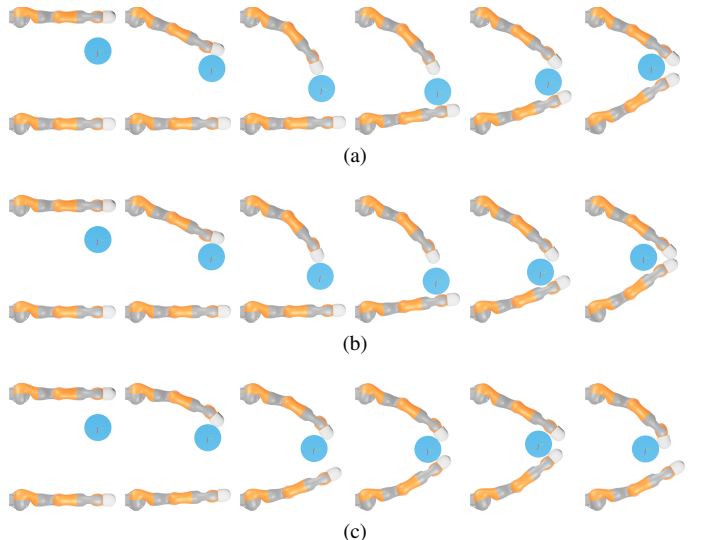


Figure 8. Example rollouts of bimanual planar bucket manipulation illustrating robot collisions under TO-CTR and their absence in our method. (a) The trajectory generated by TO-CTR under smoothed dynamics exhibits no collision. (b) Executing the TO-CTR nominal control sequence on the true hybrid dynamics leads to a robot collision. (c) Executing the policy generated by our method on the true hybrid dynamics avoids robot collision.

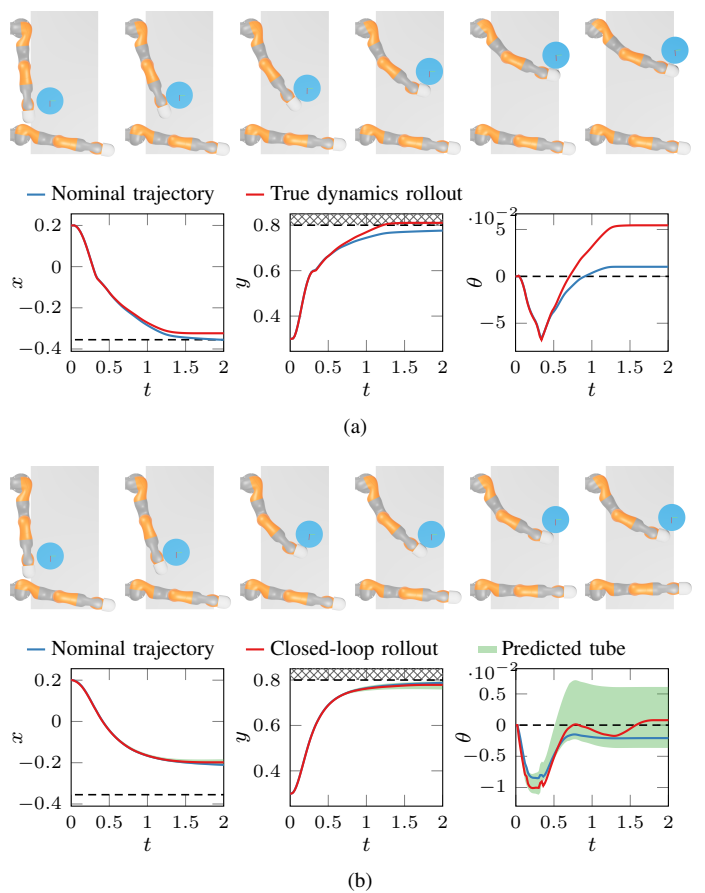


Figure 9. Example rollouts of bimanual planar bucket manipulation illustrating state constraint violations under TO-CTR and their absence in our method. Infeasible states are indicated by a cross-hatched pattern. (a) Executing the TO-CTR nominal control sequence on the true hybrid dynamics leads to bucket falling out of the table (gray region). (b) Executing the policy generated by our method on the true hybrid dynamics avoids bucket falling out of the table.